3-2021

Dynamic Holography in Resonant Nonlinear Media: Theory and Application

Jonathan E. Slagle

Follow this and additional works at: https://scholar.afit.edu/etd

Part of the Optics Commons

Recommended Citation

**Dynamic Holography in Resonant Nonlinear
Media: Theory and Application**

DISSERTATION

Jonathan Slagle

AFIT-ENP-DS-21-M-327

**DEPARTMENT OF THE AIR FORCE
AIR UNIVERSITY**

AIR FORCE INSTITUTE OF TECHNOLOGY

Wright-Patterson Air Force Base, Ohio

AFIT-ENP-DS-21-M-327

Dynamic Holography in Resonant Nonlinear Media: Theory and Application

DISSERTATION

Presented to the Faculty

Graduate School of Engineering and Management

Air Force Institute of Technology

Air University

Air Education and Training Command

in Partial Fulfillment of the Requirements for the

Degree of PhD in Optical Sciences

Jonathan Slagle, MS

January 29, 2021

AFIT-ENP-DS-21-M-327

Dynamic Holography in Resonant Nonlinear Media: Theory and Application

DISSERTATION

Jonathan Slagle, MS

Committee Membership:

Manuel R. Ferdinandus, PhD
Chair

Glen P. Perram, PhD
Member

Michael J. Havrilla, PhD
Member

AFIT-ENP-DS-21-M-327

Abstract

Two beam coupling (TBC) is a coherent interaction in which energy is transfered from one laser beam to another and has promising applications in real-time holography and coherent beam combing. We have recently shown efficient degenerate frequency TBC for counter-propagation geometries in isotropic two-photon absorbing media pumped with a nanosecond pulsed laser. When an interference pattern is generated in this media, single and two photon absorption initiates a population redistribution resulting in a holographic grating with the same modulation period and phase initially. However, due to temporal convolution of self- and cross-phase modulation, the grating will begin to shift in time relative to the interference pattern thus allowing coherent energy transfer to evolve. A comprehensive theoretical and numerical model is presented consistent with empirical results and historical observations of both energy and phase coupling. Numerical simulations indicate the presence self-oscillation due to nonlinear phase wrapping and strong excited state absorption inhibit energy transfer in a co-propagating geometry. However with proper temporal phase conditioning and choice of medium thickness, significant energy transfer can be achieved in the co-propagating case.

Table of Contents

List of Figures

List of Tables

Dynamic Holography in Resonant Nonlinear Media: Theory and Application

I. Introduction

Two-beam coupling (TBC) in Kerr media was first addressed in 1982 and 1984 with the work of Silberberg and Bar-Joseph [45, 46]. These seminal derivations involved mutually coherent fields of non-degenerate frequency interfering in a nonlinear media with a finite lifetime. Steady state solutions were provided that predict self-oscillation and instability above a certain threshold field intensity with non-reciprocal response in both energy and phase transfer. Much of the experimental observations of instability and self-oscillation at that time centered on bistable cavity systems containing Kerr media where optical feedback is present [17],[28],[16],[60],[3]. The initial work [45] centered on counter-propagating fields exclusively to illustrate the effect could occur in free-space without cavity confinement. This theory was extended [46] to include free-space interactions of any geometry including the co-propagating case and referenced the mathematical relationship to the stimulated Raman scattering. The free-space derivation was ultimately used for the textbook embodiment of Boyd [6]. Seemingly independent, Yeh followed with a steady-state derivation [62, 63] and again concluded that the phenomenon was analogous to stimulated scattering and the photorefractive effect [21]. Finally and most recently, Chi et. al. published a general model of TBC in nonlinear media in 2009 [8] to disambiguate observations in Kerr media relative to the photorefractive effect. Each derivation [46, 62, 8] has the common conclusion that steady-state models of energy transfer in Kerr media will not couple with degenerate frequency interactions. Explicit frequency detuning is required and furthermore, the optimum detuning is inversely proportional to the

time constant of the nonlinearity.

The spectral constraint imposed on Kerr media is in stark contrast with TBC in traditional photorefractive media where optimal TBC occurs for exactly the degenerate frequency case [8]. The physical reason for this lies in the locality of the nonlinearity. In Kerr media, the holographic grating occurs local to the interference pattern and the requisite dephasing occurs through the frequency mismatch. That is, the interference pattern translates with time and the grating lags due to the finite lifetime of the nonlinearity. In photorefractive media, the grating occurs non-local to the interference pattern due to charge migration and the formation of a space charge field (SCF). The resultant holographic grating evolves exactly ninety degrees out of phase corresponding the optimum phase shift for energy transfer [32, 21]. Timescales for the different cases are also important to note. While the photorefractive effect enjoys the optimum phase shift by virtue of the unique SCF physics, charge mobility is slow compared to the effectively instantaneous local effect seen in Kerr media. The obvious cost is efficiency as the product of timescale and magnitude of nonlinearity is generally held constant. This invariant is a common refrain in nonlinear optics. Specific to this work, a 2009 review article on "Nonlinear refraction and absorption: mechanisms and magnitudes" [9] references a 1986 study that concluded "to within a couple of orders of magnitude, the product (n_2 x response time) is a constant. Twenty years later, this conclusion is still valid for nonlinearities ranging over 16 orders of magnitude!" The authors use of n_2 is a generalized nonlinear refractive index. A second and equally important example is the phenomenon of "reciprocity failure" in photorefractive polymers presented by Blanche et. al. [2]. It was shown that the strength of TBC in photorefractive media decreased dramatically over nine orders of magnitude (seconds to nanoseconds) in pump pulse width.

2

1.1 Degenerate Frequency TBC with Local Gratings

Regardless of efficiency, degenerate frequency TBC in Kerr media has been observed albeit under special conditions. The process can be seeded through either self-action of the nonlinear medium or a structured frequency chirp in the field. Dutton et. al. described the first degenerate frequency TBC interaction in Kerr media in 1992 [15]. Dutton's model utilized self- and cross-phase modulation (S/XPM) as the source of frequency detuning. Because of the explicit time dependence of this self-action, the resultant system of integro-differential equations do not have simple, closed form solutions like those of the steady-state models. Numerical solutions for experimental results were provided for a co-propagating pump/probe geometry. The nonlinear media, carbon disulfide (CS_2), has a persistent lifetime on the order of 1 picosecond (psec) or about ten times shorter than the pulse width of the laser in that experiment. Coupling efficiencies were modest at less than 10%. Not surprisingly, S/XPM driven TBC was shown to have a nonlinear dependence with pump beam intensity.

Soon thereafter in 1997, a nearly identical experiment was performed with an alternate theoretical explanation. Dogariu et. al. concluded that frequency chirp in psec laser pulses was the driving force in CS_2 [13]. In this case the coupled fields can have degenerate frequency content, i.e. the pump and probe beams are derived from the same source and coupling is enabled through targeted delay relative to the nonlinear medium. Modest coupling, less than 5%, was shown to be linear with pump intensity consistent with the chirp-driven theory presented. Additionally, Tang and Sutherland published a comprehensive model involving chirp assisted TBC in 1997 [56]. Regardless of the driving force, S/XPM vs. chirp, the theoretical models provide valuable insight into how these two explanations would express themselves experimentally. In addition to the linear vs. nonlinear probe gain, the S/XPM case

3

would show a characteristic asymmetry in coupling efficiency as a function of relative time delay between pump and a weaker probe. Chirp-driven TBC on the other hand would be symmetric regardless of the pump/probe intensity ratio.

In 2001, Sylla and Rivoire provided experimental results using different polarizations of the pump laser in liquids, CS_2 and nitrobenzol, as well as solid state media, zinc selinde (ZnSe) and bismuth germanium oxide (BGO), with a co-propagating geometry [55]. Noticeably the ZnSe signal was approximately two times larger than CS_2 with the opposite sign, and noticeably asymmetric. This would be consistent with the known negative sign of free carrier refraction in ZnSe and positive sign of CS_2 molecular reorientation. Again, the coupling efficiency was relatively weak with this psec pump source.

In each of these cases the experimental work was limited to psec pulse interactions to take advantage of both the perceived nonlinear enhancement on that time scale and/or the larger spectral bandwidth provided by shorter pulses. Energy transfer in these examples was relatively weak and the phenomenon was generally treated as a deleterious effect in pump-probe spectroscopy [58].

1.2   Discovery of Degenerate Frequency Stimulated Scattering

In 2004, He et. al. published the initial work in what was named stimulated Rayleigh-Bragg scattering (SRBS) [23]. He et. al. would follow with other examples of SRBS in Kerr media [24, 25], and the proposed theoretical model was summarized in a book chapter [22]. As recently as 2019, He et. al. have extended the theory of SRBS to include the phenomenon of stimulated Mie scattering (SMS) utilizing a similar static holographic model [26, 27]. Because of the apparent degenerate frequency nature of SRBS, He et. al. proposed that the origin of the scattered field was a result of the formation of a standing Bragg grating generated from the interference

4

of a Rayleigh scattered beam, or any elastic source of backscatter, and the incident pump beam inside the nonlinear medium. The theoretical treatment followed closely to the Kogelnik derivation for thick holograms [30], but as Sutherland pointed out this would seem to violate well established TBC theory as outlined by Silberberg[46] and Yeh [62] and provided an alternative theory involving finite chirp in nanosecond pulses as the possible source of dephasing [53]. This author's work [48, 49] attempted to reconcile the theoretical discrepancy by showing the energy transfer was likely due to S/XPM-driven TBC as evidenced by the asymmetry in coupling vs. relative temporal delay consistent with Dutton et. al. [15].

Much of theoretical understanding in degenerate and non-degenerate frequency TBC in Kerr media was derived in the 1980s and 1990s [46, 62, 15, 56]. Despite the apparent disagreement of the SRBS and SMS, the physics of TBC in nonlinear media is well understood with sound theoretical footing. It would be fair to ask why it is worth revisiting now. For one, nonlinear optical media has advanced significantly since 1990s. For example, the organic dye solution used in [49] and similar materials utilized in the SUNY-Buffalo group [23, 24] have strong two-photon absorption (2PA) coupled with a strong excited state absorption (ESA), also known as an effective three photon absorbing molecule (E3PA)[54]. The population redistribution that results in ESA also generates a dynamic change in the refractive index of the medium through the Kramers-Krönig relationship (e.g. see [9] and the many references therein). It should be noted that the SRBS and SMS efficiencies along with the Fresnel coupling shown in [49] are significant compared to the antecedent work with psec pump sources. Fresnel coupling alone has been shown to exceed 60% efficiency or a amplification of approximately 15 times the probe input. This is perhaps the most intriguing reason as this would seem to break through the limitations of "reciprocity failure" mentioned previously, i.e. a highly efficient, rapid holographic amplifier. The numerous

publications in recent years by the He group at SUNY-Buffulo would indicate there is still an intense interest in degenerate frequency TBC. The progress from SRBS to SME illustrates an apparent attempt to enhance the scattering signal though material engineering. Taken together, the potential for coherent amplification, disagreement with established theory, and ongoing material design efforts indicate a strong need for a comprehensive S/XPM-driven TBC theory in 2PA/E3PA media in the nsec regime. Furthermore, the compounding and transient nature of the nonlinearity on this timescale does not afford closed-form steady state solutions [18]. Therefore, this drives an additional need for an accurate numerical simulation to provide a ground truth for further material development and transition to application.

Computational electromagnetism (CEM), or more importantly computation power, has also advanced in the last 20 years which allows us to explore interaction scenarios that would not have been possible before. For example, numerical recipes may utilize varying spectral bandwidths, spectral chirping, temporal pulse shapes, spatial distributions, and a battery optical nonlinearities ranging from near instantaneous to practically infinite. The development of nonlinear beam propagation (NLBP) [11, 44] has enabled simulation for interactions of multiple, coherent fields in contemporary nonlinear media. This will lead to a stronger ability in applying this somewhat obscure physics for a diversity of applications.

Perhaps an even better reason for revisiting degenerate frequency TBC in novel nonlinear media is the potential to address some of todays most challenging electro-optical (EO) problems. In fact many of these applications were presented early in the formulation of TBC theory [63] but have not yet been realized. In a practical sense, TBC is a coherent optical power transfer from one beam to another and has nearly innumerable photonic applications. For example, coherent beam combining can be used for power scaling or real-time holographic projection. The term coherent

is critical. This implies not only the exchange of energy but also the transfer of phase information.

1.3 Dissertation Outline and Objectives

Chapter 2 will discuss the theoretical derivation of S/XPM-driven, degenerate frequency TBC unique to 2PA/E3PA nonlinear media. While this has been generally covered in the steady-state [8], this work will present a comprehensive model including explicit contributions from well-defined nonlinearities including $\chi^{(3)}$ and population distribution. A system of coupled integro-differential equations will be presented consistent with established theory.

Chapter 3 covers the experimental and numerical methodologies. Numerical recipes for the system of coupled amplitude equation derived in Chapter 2 will be formulated. All optical geometries will be considered including co- and counter-propagation as well as the scenario where the probe field is derived from the pump through elastic scattering or more specifically derived from a Fresnel reflection. For co-propagation or single field cases, standard split step nonlinear beam propagation will be utilized [18]. For counter-propagating fields, an iterative method will be employed [44] and radial beam propagation is adopted for transverse diffraction [20] to minimize computational cost. This chapter will also describe the experimental procedures for data collection including spatial beam resolution for single beam and co-propagating embodiments. Additionally, spectral bandwidth measurements are described to further validate the degenerate frequency theory of He et. al. [22].

In Chapter 4, the experimental results will be presented as validation for the numerical model developed in Chapter 3. Unique geometrical observations will be presented for degenerate frequency TBC in 2PA/E3PA media and validated with theory. Comparison to the existing static holographic model of He et. al. will be

discussed. An attempt to observe TBC in solid state semiconductors is also addressed.

Finally, Chapter 5 offers conclusions to the work and extrapolation of TBC theory in resonant Kerr media to potential applications specifically power scaling and holographic transfer possibilities.

II. Theory

The theoretical discussion will begin with a section describing the mechanisms that govern resonant Kerr media and how these interactions effect the complex refractive index. Some contributions are effectively instantaneous on the nsec timescale of interest in this work, while others are cumulative with distinct time constants. The second section will cover the central topic of this work: the coherent nature of TBC and the how this phenomenon is enabled in nonlinear media. The derivation will be mostly classical electrodynamics with a brief discussion of quantum dynamics to illustrate the coherent nature.

Depending on the material class and timescale of interaction, numerous physical mechanisms may contribute to degenerate frequency TBC. This work will focus primarily on linear absorption and 2PA initiated population redistribution or photoionization in semiconductors and is a representative flowchart is shown in Figure 1. For reference the flowchart includes the path for space charge field generation which governs the photorefractive effect. The timescales are nominal but consistent with literature. The main purpose is to illustrate the large difference in response time of S/XPM-driven TBC relative to non-locally-driven photorefractivity.

2.1 Resonant Kerr Media

The fundamentals of nonlinear media are generally tied to the interactions of light and matter under intense radiation and has been focus of numerous textbooks [6, 37, 52, 43, 7]. Displacement of the bound electron cloud is classically considered as the source of the refractive index, also known as the radiating dipole model. Under extreme conditions, this same explanation governs perturbations to the electronic susceptibility which enables the common nonlinearities of frequency conversion,

9
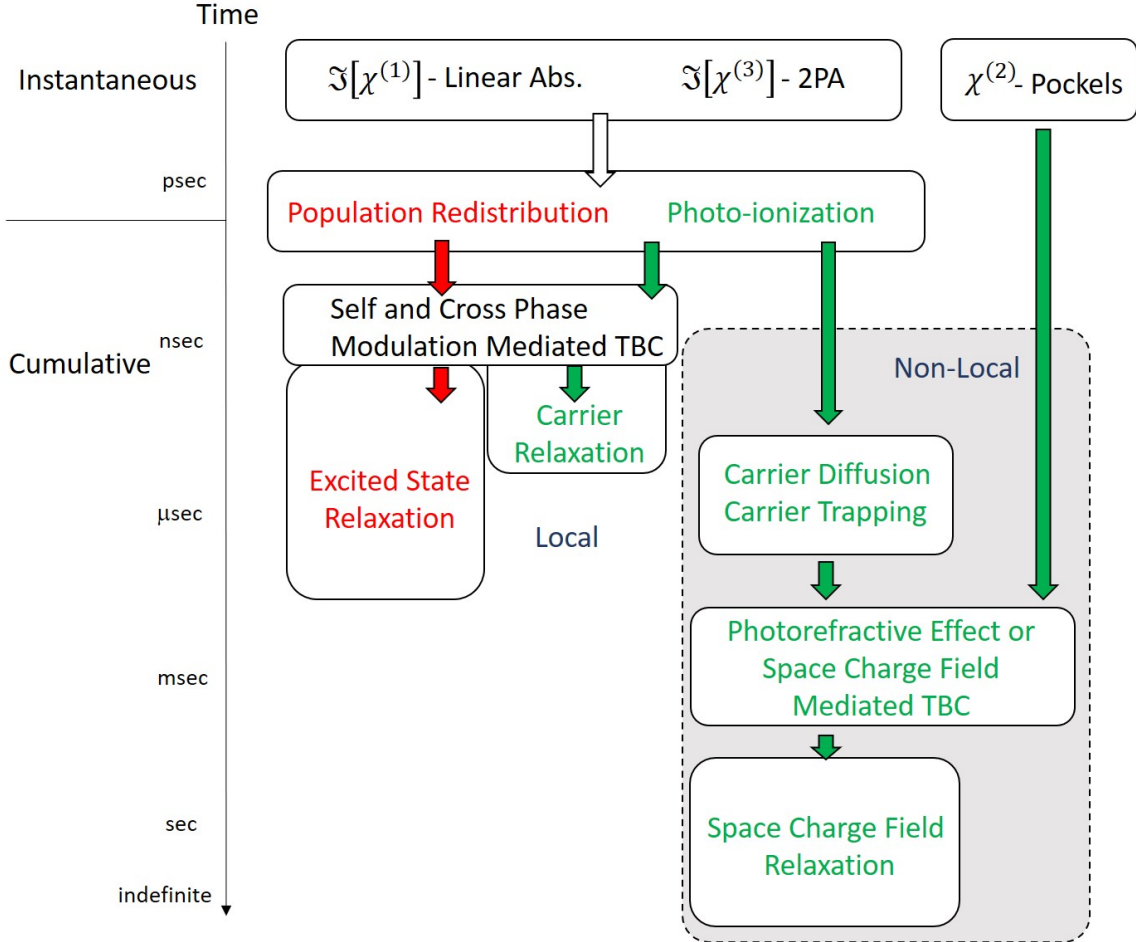
Figure 1. Possible nonlinear mechanisms for enabling TBC including local Kerr and non-local effects. By far the most common approach in the literature is the non-local photorefractive effect. However, the timescale of this mechanism results in the phenomenon of reciprocity failure [1] due to the requisite charge diffusion and limitation in carrier mobility. Conversely, the local path enabled by the imaginary parts of $\chi^{(1)}$, linear absorption, or $\chi^{(3)}$, 2PA, trigger rapid, near instantaneous coupling via a cumulative nonlinearity such as population redistribution.

two-photon absorption, and self-focusing to name a few examples. Additionally in resonant media, these bound electrons can simultaneously be excited into a manifold of higher energy electronic states each with its own persistent contribution to the complex refractive index, i.e. absorption and refraction. In some cases, extreme excitation can result in free charge carriers particularly in semiconductors or doped dielectrics which also results in a transient change to the complex refractive index of the medium. Charge carriers are then free to move and may become trapped in preferential areas resulting in non-local, static electric fields which can drive TBC by way of the second order nonlinear electronic susceptibility known as the photorefractive effect.

The Electronic Susceptibility.

The classical origins of nonlinear media is described by anharmonic response of the bound polarization in the oscillating dipole model of dielectric media and is treated as a power series expansion with the electric field as shown in equation 1 [37, 6]. For weak fields the dipole oscillation is dominated by the harmonic term and the polarization is linear. However, for strong electric fields, the dipole displacement vector is stressed due to realization of the restoring forces on the electron which introduce nonlinear components. This expanded susceptibility is then substituted into the wave equation to resolve which contributions contribute to desired nonlinear optical phenomena.

$$\vec{D} = \epsilon_0 \vec{E} + \vec{P} = \epsilon_0 \vec{E} + \epsilon_0 \chi^{(1)} \vec{E} + \epsilon_0 \chi^{(2)} \vec{E}^2 + \epsilon_0 \chi^{(3)} \vec{E}^3 + ... \tag{1}$$

The apparent Taylor series expansion of the electronic susceptibility may seem arbitrarily mathematic until we apply the symmetry conditions. For a bound electron, a real potential energy well exists that is anharmonic. The decomposition into a Taylor series expansion has material consequences which are easily provable. For

example, a material that has inversion symmetry must satisfy the following equation with respect to electric displacement

$$U(X) = U(-X) = \frac{1}{2}m\omega_0^2 X^2 + \frac{1}{2}amX^3 + \frac{1}{4}bmX^4... \tag{2}$$

which requires the first order correction (or second order electronic susceptibility) must be equal to zero. As a result, centrosymmetric media simply cannot generate a $\chi^{(2)}$ response and will not allow for parametric frequency conversion. This imparts a very real physical consequence that to achieve second order effects, the material must be non-centrosymmetric. Furthermore, because the effect is weak, this symmetry requirement must be maintained over large physical distances to enable the practical realities of the Pockel's effect and frequency conversion which requires the additional complication of phase matching. The physical consequence of this is that second order effects such as frequency conversion must occur in media with large scale order. This is easily demonstrated empirically as almost all commercial examples of frequency conversion are performed in crystalline media. For classical derivation of the symmetry rules governing the second order nonlinear susceptibility, see Ref. [37].

The third order nonlinear susceptibility (second order correction in Equation 2), and higher odd orders, on the other hand can exist in centrosymmetric media including isotropic liquids. The primary consequence of this is that the nonlinear coefficient for third order effects is substantially smaller than the second order and requires more intensity, or irradiance, for observation. The third order nonlinear susceptibility can also be complex valued. With the imaginary part contributing to two-photon absorption and its real part governing the instantaneous Kerr effect. Both cases are automatically phased matched resulting in an intensity dependent complex refractive index. For a single input beam, the complex amplitude equation for a third order

12
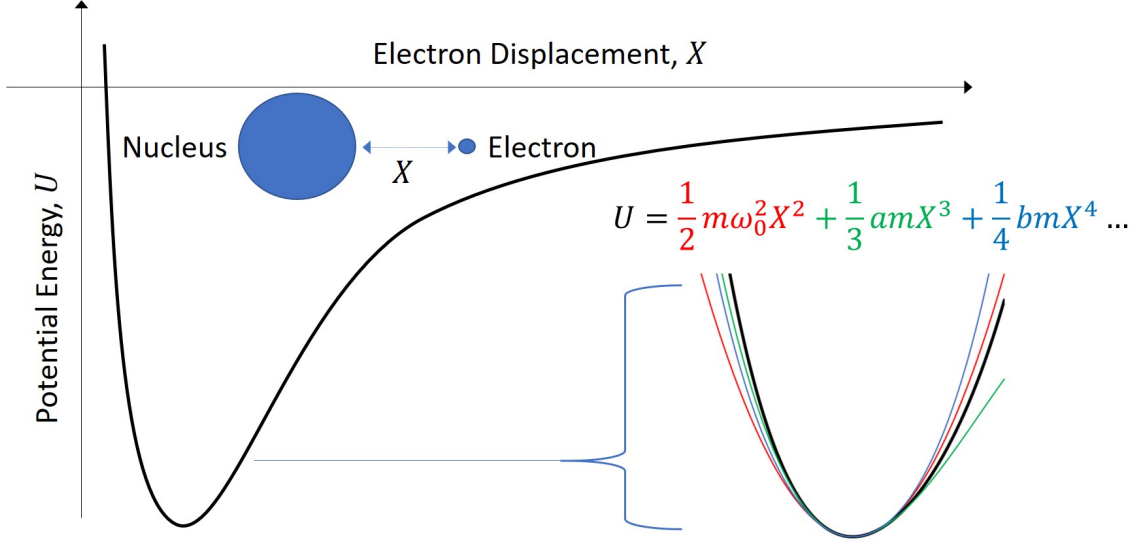
Figure 2. Anharmonic nature of bound electrons that originates the nonlinear electronic susceptibility. In this simple ball and string illustration, the potential energy well is distorted due to restoring or repulsive forces as the electron is pushed away from equilibrium. This function can be projected onto a polynomial basis where each correction contributes to unique phenomena in nonlinear optics and explains the symmetry rules governing those effects.

nonlinearity is expressed as

$$\frac{dA}{dz} = i\chi^{(3)}|A|^2 A. \tag{3}$$

If we define $\chi^{(3)}$ as

$$\chi^{(3)} = i\frac{2\pi}{\lambda}\gamma - \frac{\beta}{2} \tag{4}$$

where γ and β are the Kerr and 2PA coefficients, respectively. Substitution of 4 into 3 followed by conversion into irradiance and phase equations utilizing the equality of

$$\frac{dA}{dz} = \frac{d\sqrt{I}}{dz}\exp(i\phi) + i\sqrt{I}\exp(i\phi)\frac{d\phi}{dz} \tag{5}$$

and

$$A = \sqrt{I}\exp(i\phi) \tag{6}$$

provides the canonical irradiance and phase equations of

$$\frac{dI}{dz} = -\beta I^2,\tag{7}$$

and

$$\frac{d\phi}{dz} = \frac{2\pi}{\lambda}\gamma I,\tag{8}$$

respectively. Equation 7 describes 2PA and represents loss. Equation 8 governs self-phase modulation (SPM). For two beams, the coupled amplitude equation becomes

$$\frac{d}{dz}\begin{bmatrix} A_1 \\ \pm A_2 \end{bmatrix} = i\chi^{(3)}\begin{bmatrix} |A_1|^2 + 2|A_2|^2 & 0 \\ 0 & |A_2|^2 + 2|A_1|^2 \end{bmatrix}\begin{bmatrix} A_1 \\ A_2 \end{bmatrix}\tag{9}$$

with the plus or minus of A_2 dependent on co- or counter-propagation, respectively. Similarly, equation 9 may also be written in terms of irradiance and phase as

$$\frac{d}{dz}\begin{bmatrix} I_1 \\ \pm I_2 \end{bmatrix} = -\beta\begin{bmatrix} I_1 + 2I_2 & 0 \\ 0 & I_2 + 2I_1 \end{bmatrix}\begin{bmatrix} I_1 \\ I_2 \end{bmatrix}\tag{10}$$

and

$$\frac{d}{dz}\begin{bmatrix} \phi_1 \\ \pm\phi_2 \end{bmatrix} = \frac{2\pi}{\lambda}\gamma\begin{bmatrix} I_1 + 2I_2 & 0 \\ 0 & I_2 + 2I_1 \end{bmatrix}.\tag{11}$$

In addition to the single beam terms, the two beam case now has coherent absorption and cross-phase modulation (XPM) terms and are only present when the electric fields have parallel polarizations. It should also be noted that on the timescales relevant to this work, S/XPM derived from the Kerr nonlinearity is generally swamped by the cumulative effects discussed in the next section and is often neglected. By itself, 2PA is also a weak effect however its contribution to the source terms in the cumulative nonlinearities is critically important.

14

Cumulative Population Redistribution.

For all the cases presented in this work so far, nonlinear effects originating from the displacement of the electron cloud, or radiating dipole model (electronic susceptibility), are considered instantaneous or much, much faster than a nsec laser pulse. As perturbations, these contributions are generally weak. However, these effects can seed further cumulative nonlinearities generating local and non-local changes to the refractive index. For example in the work or Dogariu [13], the physical manifestation of the nonlinear refractive index was the reorientation of solvent dipoles in carbon disulfide. The atomic movement does not decay instantaneously providing the requisite persistent nonlinearity for TBC in that case. Molecular reorientation of this kind has a decay on the order of a few psec. The compounding nature of cumulative nonlinearities is such that longer lifetimes lead to larger changes in the refractive index as one might expect through the convolution integral. As a result, the total refractive index change for molecular reorientation is relatively small. In contrast, resonant effects by way of population redistribution can be substantial.

For semiconductor media, photoexcitation of free carriers into the conduction band results in a overall change in the optical properties. These values can be approximated through first principles [31] or with semi-empirical approaches [9]. The physical model is defined by the Drude-Lorentz theory. Promotion of a free carrier into the conduction band results in a change in conductivity which leads to a change in the dielectric constant and therefore a change in the complex refractive index. This photoexcitation can be achieved from linear absorption or via 2PA (imaginary $\chi^{(3)}$). Once in the conduction band, these carriers will eventually decay back to the valence band by way of recombination or Auger annihilation. If the lifetime of the carriers in the conduction band is long compared to the excitation pulse, a significant population will accumulate creating a bulk change in the complex refractive index. This change

in refractive index can be significant has been extensively studied [19, 57, 41].

In contrast to semiconductor physics, organic media are for the most part insulating even under intense laser radiation. Even in the case of ionization, charge mobility is generally poor and recombination occurs rapidly. The electro-optical utility of organic dielectrics lies in the redistribution of bound electronic transitions as outlined in Figure 3. Each excited state contributes a different complex refractive index. As light is absorbed, either by 1PA or 2PA, the excitons (excited molecules) will cascade through the various higher energy states according to the temporal dynamics associated with state lifetime. The material benefit of this model is that some of these states particularly the forbidden triplet states (T_n) can have lifetimes in the 100s of microseconds or even longer under the right conditions [54, 40, 39].
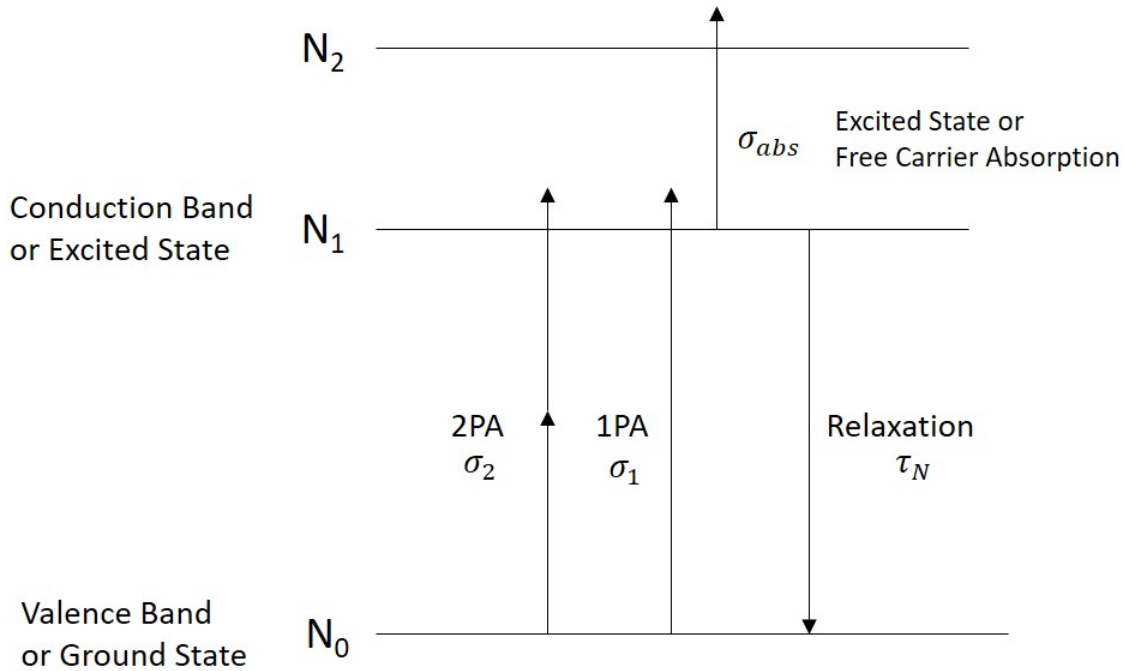
Figure 3. The Jablonski diagram outlines the population redistribution pathways for organic and semiconductor, i.e resonant Kerr, media. Excited states or free-carriers may be promoted into the excited state manifold or conduction band by either one or two photon excitation where they will persist with a finite lifetime, τ_N. In this state, the particles contribute changes to the total complex refractive index leading to nonlinear refraction or absorption.

Population redistribution plus charge diffusion leads to space charge field which can drive the second order nonlinearity. Automatically phase shifted grating and interference pattern leads to efficient TBC however the process is generally slow due to charge mobility. Furthermore, in the cases presented here, the organic media is purely isotropic without a $\chi^{(2)}$. Even if free charges are generated and diffuse to form a SCF, there is no second order nonlinearity available to initiate the photorefractive effect.

Transient population redistribution can lead to changes in bulk optical properties [54, 52]. As the pulse propagates through the medium, bound electronic transitions can occur or free carriers are generated through photo-excitation. This process can be triggered by way of single photon or two-photon absorption (1PA or 2PA). If it were possible to excite all ground state dipoles or valence band electrons were into an excited state or conduction band, the result would be an entirely different dielectric material with a new refractive index and absorption properties. This is of course not possible but each instance of excitation results is some small change in the complex refractive index, $\Delta \tilde{n}$, such that

$$\Delta \tilde{n} = \sum_{j=0}^{n} \left(\frac{\sigma_{abs,j}}{2} + i \frac{2\pi \sigma_{ref,j}}{\lambda_0} \right) N_j \tag{12}$$

where each state has its own absorption and refraction cross sections, σ_{abs} and σ_{ref} respectively.

This allows for easy expansion of the population dynamics to account for three and four level systems such as those found in gain media. One need only to define the excitation and decay terms for each state. It is also possible to add inter-particle terms such as excited state annihilation and Auger recombination if necessary [35]. However for most cases, we can approximate the population dynamics with a simple two level model with a ground state (or valence band), N_0, and excited state (conduction band)

population, N, such that

$$\frac{dN}{dt} + \frac{N}{\tau_N} = \frac{\alpha I}{h\nu} + \frac{\beta I^2}{2h\nu}. \tag{13}$$

where α and β are the 1PA and 2PA coefficients and τ_N is the lifetime of the excited state or free carrier. For example, E1BTF is a well-characterized 2PA organic dye with spectral features shown in Figure 4 [40]. In this example, the ground state in a singlet, S_0 or equivalent to N_0 in Figure 3. The first excited state is also a singlet, S_1, which undergoes rapid intersystem crossing (sub psec) to the first excited triplet state, T_1. Due to the high triplet state quantum yield, ϕ_T, and the rapid excited singlet decay, this molecule can be appropriately model as a two-level system with T_1 replacing N in Equation 13. Saturation can be enforced by expanding α and β and
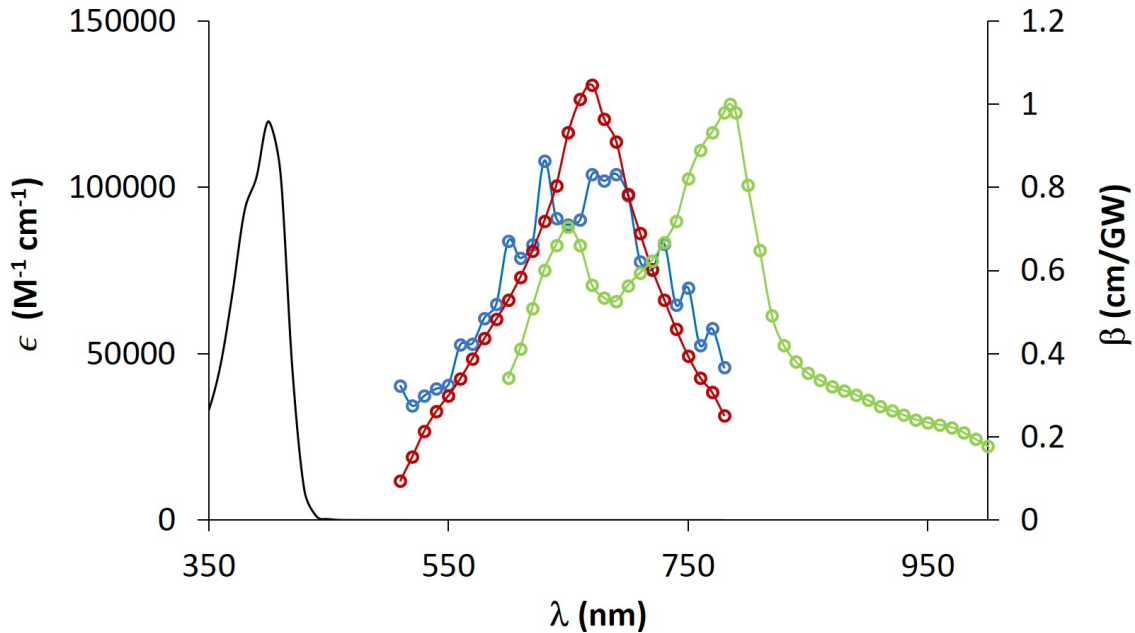
Figure 4. Ground, excited state and two-photon absorption coefficient spectra for E1BTF in solution [40]. While these spectra represent absorption and loss, nonlinear refraction accompanies these effects through the Kramers-Kronig relation [9]. Quantification of the population contributions to the nonlinear refractive index is challenging especially for organic solutions and generally measured experimentally. Note that the values for β assume a ground state concentration of 50 mM.

forcing conservation of mass such that

$$\alpha = \sigma_1 N_0, \quad \beta = \sigma_2 N_0, \quad N_0 = N - N_{initial} \tag{14}$$

where $N_{initial}$ is the starting ground state population density and σ_1 and σ_2 are the 1PA and 2PA absorption cross sections respectively. This is often necessary for solutions of organic media or traditional photorefractive crystals where the concentration of active molecules or donor/trap densities may be limited. That is, the 1PA and 2PA coefficients are not constant. For semiconductors, the density of states is generally large and saturation is not considered. For these cases, we will use the terms α_0 and β_0 to denote their constant values. For the two-level model, the nonlinear contributions are thus

$$\alpha_{NL} = \sigma_{abs} N, \quad n_{NL} = \sigma_{ref} N \tag{15}$$

with σ_{abs} taking the value of T_1 in our E1BTF example. Note that organic spectra are often reported as molar extinction coefficients. The conversion from ϵ in units of $M^{-1}cm^{-1}$ to σ in units of cm^2 is simply

$$\sigma = 3.82 x 10^{-21} \epsilon. \tag{16}$$

Thermal Refraction.

When excited states or free carriers decay non-radiatively, this results in thermal accumulation in the media resulting in a thermo-optic effect. This process can be quite complicated involving acoustic driven density changes in organic liquid samples [9, 34] and various temperature dependent dynamics in semiconductors [31]. Since these thermo-refractive effects are subject to both acoustic transport and diffusion, a general understanding of the processes are necessary to properly scope the efficacy

19

for the timescale of interest.

In organic liquids, we can express the thermal time dynamics as

$$\rho C \frac{d\Delta T}{dt} - \kappa \nabla^2 \Delta T = \alpha I + \sigma_{abs} N I + \beta I^2 \qquad (17)$$

where ΔT is the change in temperature, ρ is the density, C is the heat capacity, and κ is the thermal diffusivity.

In semiconductor media, virtually every optical property is subject to change in temperature owing to the thermo-chromism of the bandgap. This in turn effects the cross-sections of free-carrier absorption and refraction. Acoustic transport in solid state is generally considered one order of magnitude weaker than for liquids. As a result, the lifetime of this nonlinearity is governed by diffusion which would have a time constant, and transit time much longer than the nsec pulse width.

While this general understanding of thermal refractive process are insightful, in practice comprehensive numerical modeling is computationally intensive particularly in the effects of non-locality. As a result a more direct phenomenological approach is adopted. Experimental measurements often report the change in refractive index as a single value lumping all cumulative effects together. For example, utilizing large differences in pulse width allows one to resolve instantaneous effects separate from cumulative effects [47].

2.2 Two Beam Coupling in Resonant Kerr Media

In the most general case assuming parallel polarization, two mutually-coherent, interacting waves have a total electric field of

$$\vec{E} = A_1 \exp\left[i\left(\vec{k_1} \cdot \vec{r} - \omega_1 t\right)\right] + A_2 \exp\left[i\left(\vec{k_2} \cdot \vec{r} - \omega_2 t\right)\right] + c.c. \qquad (18)$$

where $|k_j| = \frac{2\pi n_0}{\lambda_j}$ with n_0 equal to the real, linear refractive index of the medium and λ_j is the wavelength of light of the jth beam in vacuum. The optical frequencies are designated by ω_j and the complex amplitudes are A_j with $j = 1, 2$. To relate this field to experimental data, we define the complex amplitudes as

$$A_j = \sqrt{I_j} \exp\left(i\phi_j\right) \tag{19}$$

where I_j is the irradiance of the field (in W/cm^2). Equation 18 has a total irradiance of

$$I = I_1 + I_2 + \{A_1 A_2^* \exp\left[i\left(\vec{q} \cdot \vec{r} - \delta t\right)\right] + c.c.\} \tag{20}$$

or,

$$I = I_S + 2\sqrt{I_1 I_2} \cos(\vec{q} \cdot \vec{r} + \Delta\phi - \delta t) = I_S + I_O \tag{21}$$

with grating vector $\vec{q} = \vec{k_1} - \vec{k_2}$, frequency difference $\delta = \omega_1 - \omega_2$, and phase shift $\Delta\phi = \phi_1 - \phi_2$. This represents an interference pattern resulting from the overlap of mutually coherent electric fields with a static term, $I_S = I_1 + I_2$, and an oscillating term, I_O. If the fields are degenerate frequency, $\delta = 0$ and $\Delta\phi$ is constant, the interference pattern if fixed, i.e. a standing wave. However, if $\delta \neq 0$ and/or $\Delta\phi$ is a function of time, the pattern translates along the direction of $\vec{q}$ either forward or backward depending on the signs of the time dependent terms. In general, the amplitude and irradiance variables in Equation 19 are functions of both time and space transverse to the direction of propagation, e.g. Gaussian temporal and spatial profiles propagating in the direction of $\vec{k_j}$. Additionally, the phase variables can also be functions of time and space, e.g. the quadratic phase of a converging beam or more complicated holographic patterns, and temporal phase resulting from S/XPM.

Figure 5 illustrates Equation 21. In subfigure a), the fields are co-propagating in the $+z$ axis with $\theta_1 = -\theta_2$. As a result, the grating vector, $\vec{q}$, is purely in the

$\hat{x}$ plane. In contrast, subfigure b) shows counter-propagating field with equal angles which results in a grating vector purely in the $\hat{z}$ plane. If $\theta_1 \neq \theta_2$, the grating vector would point somewhere in the $\hat{x}\hat{z}$ plane according to the vector subtraction definition of $\vec{q}$. The grating wavenumber for co-propagation (designated by +)is then defined as [8]

$$|\vec{q}|_+ = \frac{4\pi \sin(\frac{\theta_1 - \theta_2}{2})}{\lambda} \tag{22}$$

where we have set $\lambda_0 = \lambda_1 = \lambda_2$ which is a valid assumption for the cases considered in this work since for non-degenerate frequency interactions, δ is limited to the order of one GHz and $\Delta\lambda$ is negligible. The grating wavenumber is inversely proportional to the period or wavelength of the interference pattern. As a result, small angles lead to large interference pattern wavelengths which have some consequences in traditional photorefractive media which rely on non-local effects such as carrier mobilities to enable beam coupling [21]. Small angles also lead to small wavenumbers for co-propagation which we will show contributes to efficiency issues in Kerr-driven TBC for different reasons. Alternatively, counter-propagation (-) has the opposite effect with respect to angle as demonstrated by

$$|\vec{q}|_- = \frac{4\pi \cos(\frac{\theta_1 - \theta_2}{2})}{\lambda}. \tag{23}$$

For this geometry the wavenumber is larger for smaller angles.

If this interference pattern occurs in a nonlinear medium, $\tilde{n}_{NL}$, its structure may be transfered in the form of a holographic grating. Under the proper conditions, this is one of the enabling features for TBC.
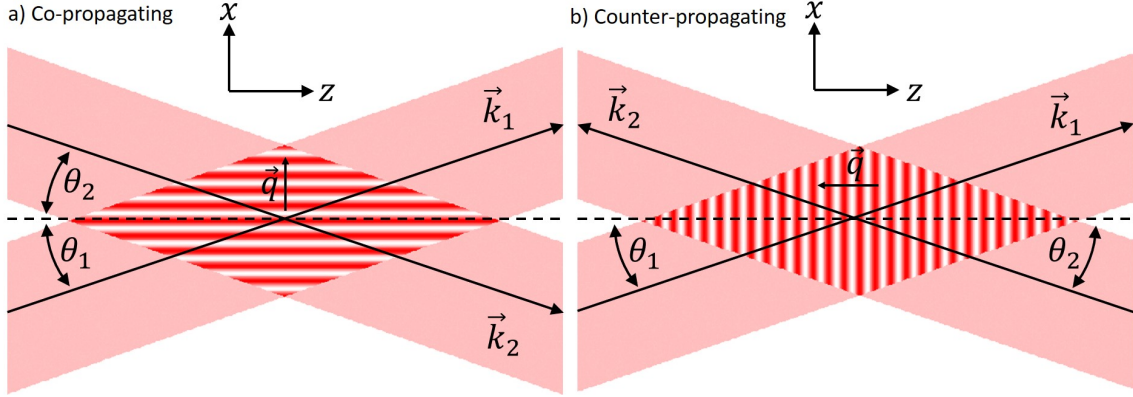
Figure 5. Interference pattern for (a) co- and (b) counter-propagating fields. As the grating wavenumber decreases, i.e. small angles of incidence, the interference pattern period increases. This leads to angular sensitivity for TBC in media relying on nonlocal mechanism such as the photorefractive effect. If these patterns are transferred to the nonlinear medium, light can scattering according to the grating vector geometry.

Temporal Convolution.

The existence of a holographic grating is by itself insufficient to insure energy exchange for two mutually coherent fields. That is, if the interference pattern and the resultant refractive index grating are exactly in phase the fields will pass through without exchanging energy. It should be noted that this is also true for nonzero δ or a time dependent $\Delta\phi$. That is, if the pattern is travelling at the same velocity as the grating, they are still in phase and again, no energy coupling will occur. This phenomenon can and will be derived in subsequent chapters from classical electromagnetism, but the Quantum Electrodynamics explanation provides a more descriptive illustration shown in Figure 6. When the fields are exactly in phase the probability of scattering in either direction is logically equal and the net effect is zero coupling. When they are out of phase less than 180 degrees, symmetry is broken, the probabilities are not equal, and one field will be favored over the other. At 90 degrees the asymmetry is maximum and therefore is the ideal case for TBC. At 180 degrees the probabilities are again equal. Greater than 180 but less than 360, the preferred field

changes and finally at 360 the process repeats.

$\Delta\phi = 0$ $0 < \Delta\phi < \dfrac{\pi}{2}$ $\Delta\phi = \dfrac{\pi}{2}$ $\dfrac{\pi}{2} < \Delta\phi < \pi$ $\Delta\phi = \pi$

$\pi < \Delta\phi < \dfrac{3\pi}{2}$ $\Delta\phi = \dfrac{3\pi}{2}$ $\dfrac{3\pi}{2} < \Delta\phi < 2\pi$ $\Delta\phi = 2\pi$
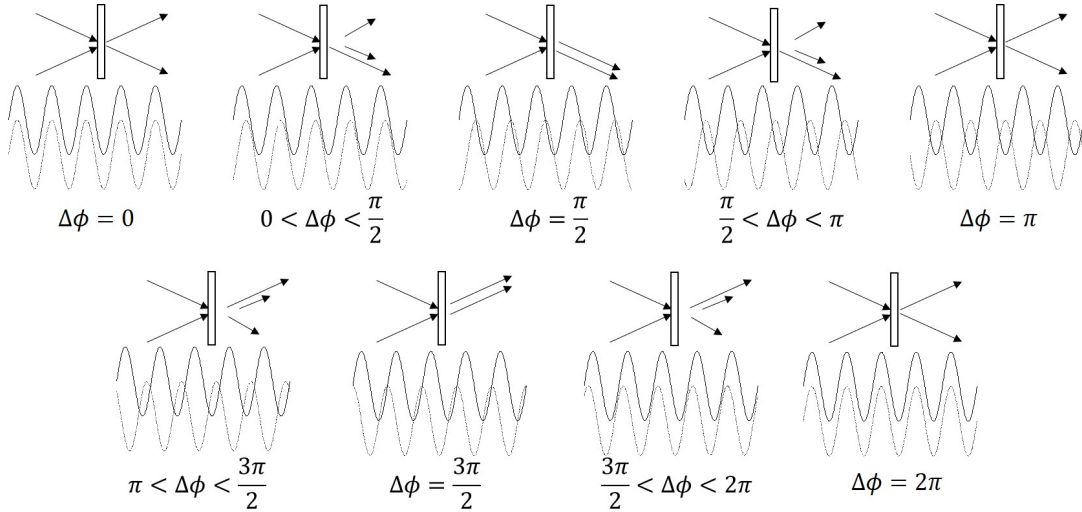
Figure 6. Quantum electrodynamic illustration of the coherent interaction of the interference pattern (solid line) with the induced grating (dashed line). TBC is fundamentally coherent. When the grating and pattern in phase or exactly π out of phase, the net effect is zero energy exchange. For asymmetric interactions, one field will be favored over the other and TBC can occur.

The magnitude and direction depend on the medium. The photorefractive effect is one well documented example and takes advantage of non-local formation of space-charges [61, 32, 21]. Alternatively, TBC may be generated by means of a nonlinearity that has a finite lifetime where the grating is formed locally, i.e. requires no charge transport, and will be the subject of the following derivation consistent with Refs. [46, 62, 8]

A persistent nonlinearity provides one important function critical for TBC by convolving the source term or forcing function of the interference pattern with the time decay of the nonlinearity. A good example that has already been introduced and used throughout the remainder of this work is population redistribution. The simplest example is a non-saturating two level model where the excited state has the temporal nature of

$$\frac{dN}{dt} + \frac{N}{\tau} = f\left[I(t)\right]. \tag{24}$$

24

where N is the population density in the excited state (or the number of free carriers), τ is the lifetime, and f is the source term that is a dependent on irradiance and time. It is therefore also function of both the static and oscillating terms of the total irradiance defined by Equation 21. Different classes of media may have very different source terms. Regardless of the structure of f, Equation 24 has the analytical solution of

$$N = \int_{-\infty}^{t} f\left[I(t')\right] \exp\left(\frac{t'-t}{\tau}\right) dt' \tag{25}$$

which we recognize as a convolution of the source term with an exponential decay. It should also be noted that in practice the medium may have multiple contributions to the nonlinear refractive index with different time constants in which case Equation 25 becomes a sum of convolutions [50]. For the sake simplicity we will consider a medium with only one time constant. If we define a causality function $D(t)$ such that

$$D(t) = \begin{cases} \exp\left(-t/\tau\right) & t >= 0 \\ 0 & t < 0 \end{cases}, \tag{26}$$

we can then rewrite Equation 25 as

$$N = f * D \tag{27}$$

where the $*$ denotes a convolution of two functions.

The source term, f, is a function of the total irradiance, Equation 21, it will have a stationary (S) term and an oscillating (O) terms. In general, the source term may be represented as a power series expansion of irradiance such that

$$f = aI + bI^2 + ... = aI_S + bI_S^2 + 2bI_S I_O + aI_O + bI_O^2 + ... \tag{28}$$

where the coefficients a and b represent the material response, e.g. the single and two photon absorption present in Equation 13. Higher order terms can be added as necessary.

The population can be solved by substituting Equation 28 into Equation 27 and distributing the convolution across each source term. The phenomenon illustrated in Figure 6 can now be demonstrated mathematically. Consider just the contribution from the linear oscillating term, aI_O. Applying the definition of I_O from Equation 21 gives oscillating population grating of

$$N_{osc} = \left\{ \sqrt{I_1 I_2} \exp\left[i(\Delta\phi - \delta t)\right] * D \right\} \exp\left(i2k_0 x\right) + c.c. \tag{29}$$

where we have assumed small angles of incidence such that $\theta_1 = -\theta_2$ placing the interference pattern entirely in the $\hat{x}$ plane for the counter-propagating geometry(see Figure 5). If the phase shift, $\Delta\phi$ compounds over time due to S/XPM convolved with the decay function or the frequencies are non-degenerate $(\delta \neq 0)$, the population, i.e. the refractive index grating, with shift. Compare this to the interference pattern, I_O, in the same form,

$$I_O = \sqrt{I_1 I_2} \left\{ \exp\left[i\left(2k_0 x + \Delta\phi - \delta t\right)\right] + c.c. \right\}, \tag{30}$$

and it becomes evident that the local grating will shift away from the interference pattern. This de-phasing is not instantaneous but rather evolves through time. As we have already discussed, Equation 30 describes an interference pattern that is traveling for nonzero δ or a time-dependent $\Delta\phi$. The refractive index grating which is proportional to the population also travels in $\hat{x}$ but lags due to the convolution integral. This can be illustrated by expressing the interference pattern and grating as time dependent phasors shown in Figure 7. If we assume an effectively infinite time

constant, τ_N, we can visualize this convolution as a series of vector additions. From this perspective it is easy to see how these phasors will drift away from one another over time.
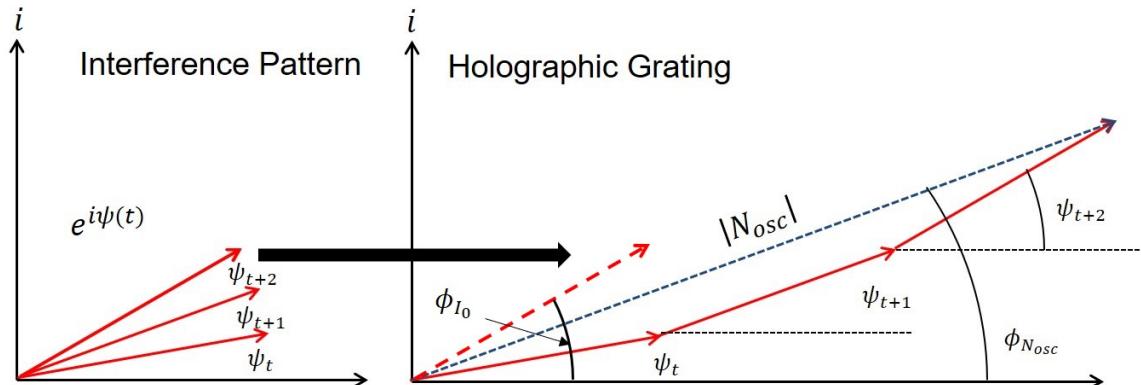
Figure 7. Phasor representation of the interference pattern compared to the refractive index grating driven by the temporal convolution of population oscillation, N_{osc}, where ψ represents the full time dependent argument of the interference pattern. For effectively infinite time constants, we can visualize this a series of vector additions in the hologram for each time step. From this exercise it is apparent the relative phases will drift over time.

Nonlinear Coupled Wave Equation.

The next step is to expand the nonlinearity to include absorption and define the total complex refractive index as

$$\tilde{n} = n_0 + n_{NL} + \frac{i}{2k_0}\left(\alpha_0 + \alpha_{NL}\right) \tag{31}$$

where n_0 and α_0 are the linear refractive and absorptive contributions respectively, n_{NL} is the real part of the nonlinear refractive index defined by Equation 31, and $k_0 = \frac{2\pi n_0}{\lambda_0}$. The nonlinear absorption, α_{NL}, and refraction terms, n_{NL}, are both convolution integrals. In the case of population redistribution, the real and imaginary contributions share a common source and can be combined for simplicity which we will cover in later sections. Since the nonlinear contributions act as a perturbations,

27

we can write the square of the total complex index to a good approximation as [8]

$$\tilde{n}^2 \approx n_0^2 + 2n_0 n_{NL} - i\frac{n_0\lambda_0}{2\pi}\left(\alpha_0 + \alpha_{NL}\right).$$

(32)

Finally, the system must satisfy the wave equation such that

$$\nabla_\perp^2 \vec{E} + \frac{\partial^2 \vec{E}}{\partial z^2} - \frac{1}{c^2}\frac{\partial^2}{\partial t^2}(\tilde{n}^2 \vec{E}) = 0$$

(33)

with $\nabla_\perp^2$ representing transverse diffraction. Inserting the total field, Equation 18 and applying the slowly varying envelope approximation (SVEA) to the second order derivatives of z [52] provides

$$\frac{\partial^2 \vec{E}}{\partial z^2} = \left(2ik_1\frac{\partial}{\partial z} - k_1^2\right)A_1 \exp\left[i\left(k_1 z - \omega_1 t\right)\right] + \left(2ik_2\frac{\partial}{\partial z} - k_2^2\right)A_2 \exp\left[i\left(k_2 z - \omega_2 t\right)\right]$$

(34)

assuming that propagation of either field is limited to small angles of incidence and primarily in the $\pm\hat{z}$ direction. Equation 34 may be simplifed by assuming $\lambda_0 = \lambda_1 = \lambda_2$ and therefore $k_0 = k_1 = \pm k_2$ for the scalar terms. Equation 34 then becomes

$$\frac{\partial^2 \vec{E}}{\partial z^2} = 2ik_0\left\{\frac{\partial A_1}{\partial z}\exp\left[i\left(k_1 z - \omega_1 t\right)\right] \pm \frac{\partial A_2}{\partial z}\exp\left[i\left(k_2 z - \omega_2 t\right)\right]\right\} - k_0^2 E$$

(35)

with the $\pm$ determining the $(+)$ co- or $(-)$ counter-propagating cases. A similar SVEA is applied to the second order time derivative to give

$$\frac{1}{c^2}\frac{\partial^2}{\partial t^2}(\tilde{n}^2 \vec{E}) = -\frac{2i\omega\tilde{n}^2}{c^2}\frac{\partial \vec{E}}{\partial t} - \frac{\omega^2\tilde{n}^2}{c^2}\vec{E}$$

(36)

assuming $\omega = \omega_1 = \omega_2$ in the scalar terms and omitting the negligible contributions from the explicit time dependence in the embedded convolution integrals. Substitut-

ing Equations 35, and 36 into Equation 33 provides

$$-i\frac{\nabla_\perp^2 \vec{E}}{2k_0} + \frac{\partial A_1}{\partial z}e^{i(k_1 z - \omega_1 t)} \pm \frac{\partial A_2}{\partial z}e^{i(k_2 z - \omega_2 t)} + \frac{\tilde{n}^2}{n_0 c}\frac{\partial \vec{E}}{\partial t} + i\frac{\omega^2}{2k_0 c^2}(n_0^2 - \tilde{n}^2)\vec{E} = 0. \quad (37)$$

Next, Equation 32 is substituted into Equation 37 gives

$$\frac{\partial A_1}{\partial z}e^{i(k_1 z - \omega_1 t)} \pm \frac{\partial A_2}{\partial z}e^{i(k_2 z - \omega_2 t)} + \frac{1}{\nu_p}\frac{\partial \vec{E}}{\partial t} = i\frac{\nabla_\perp^2 \vec{E}}{2k_0} - \frac{\alpha_0}{2}\vec{E} + \left(\frac{\alpha_{NL}}{2} - i\frac{2\pi}{\lambda_0}n_{NL}\right)\vec{E} \quad (38)$$

assuming $\frac{\tilde{n}^2}{n_0 c} \approx \frac{1}{\nu_p}$ where ν_p is the phase velocity.

The partial time derivative can be eliminated by switching from the laboratory frame to the local pulse frame such that[11]

$$
\begin{aligned}
z' = z, \qquad &t' = t - \tfrac{z}{\nu_p}, \\
\frac{\partial}{\partial z} = \frac{\partial}{\partial z'} - \frac{1}{\nu_p}\frac{\partial}{\partial t'}, \qquad &\frac{\partial}{\partial t} = \frac{\partial}{\partial t'}.
\end{aligned}
\tag{39}
$$

This is a trivial substitution for the co-propagating case however special care will need to be taken for the counter-propagating case in the numerical analysis. Equation 38 is now

$$\frac{\partial A_1}{\partial z'}e^{i(k_1 z' - \omega_1 t')} \pm \frac{\partial A_2}{\partial z'}e^{i(k_2 z' - \omega_2 t')} = i\frac{\nabla_\perp^2 \vec{E}}{2k_0} - \frac{\alpha_0}{2}\vec{E} + \left(i\frac{2\pi n_{NL}}{\lambda_0} - \frac{\alpha_{NL}}{2}\right)\vec{E} \quad (40)$$

where the first two terms on the right-hand side govern the transverse diffraction and linear absorption. The final step is to evaluate the last term to determine the nonlinear and beam coupling operations.

By substituting the nonlinearity definitions for the two-level population redistribution model, Equation 15, into Equation 40, the final term becomes

$$\left(i\frac{2\pi n_{NL}}{\lambda_0} - \frac{\alpha_{NL}}{2}\right)E = \left(i\frac{2\pi \sigma_{ref}}{\lambda_0} - \frac{\sigma_{abs}}{2}\right)NE = \sigma_{NL}NE \quad (41)$$

29

where N is the population of excited states or free-carriers. Recall that N is a convolution integral, Equation 27, and also a function of the forcing terms, Equation 28, containing both stationary and oscillatory contributions. Distributing the convolution integral across the source terms gives

$$NE = [(aI_s + bI_S) * D] E + \{[(2bI_S + a) I_O] * D\} E + [(bI_O^2) * D] E. \qquad (42)$$

The first term in Equation 42 will drive typical excited state or free carrier absorption and refraction similar to the single beam case. The second and third terms govern the interaction between the interference pattern of the electric fields and the population grating which in turn drives the complex refractive index grating. Recalling the definition of I_O from Equation 21, the convolution integral in the second term of 42 can be rewritten as

$$[(2bI_S + a) I_O] * D = \left\{ (2bI_S + a) \sqrt{I_1 I_2} \exp\left[i\left(\vec{q} \cdot \vec{r} + \Delta\phi - \delta t\right)\right] + c.c. \right\} * D. \quad (43)$$

The spatial component can be pulled out of the temporal convolution allowing for a simpler expression. Combining all time-dependent terms into N_{osc} provides

$$[(2bI_S + a) I_O] * D = N_{osc}^{(1)} \exp\left[i\vec{q} \cdot \vec{r}\right] + c.c. \qquad (44)$$

with the time dependent amplitude defined as

$$N_{osc}^{(1)} = \left[(a + 2bI_S) \sqrt{I_1 I_2} e^{i(\Delta\phi - \delta t)} \right] * D. \qquad (45)$$

Similarly, the final term in Equation 42 will have an oscillating component. However in this case, the forcing function is quadratic and the interference pattern result-

ing from this term is

$$I_O^2 = 4I_1 I_2 \cos^2 (\vec{q} \cdot \vec{r} - \delta t + \Delta \phi) = I_1 I_2 \left[e^{2i(\vec{q} \cdot \vec{r} - \delta t + \Delta \phi)} + c.c. + 2 \right]. \qquad (46)$$

Note the additional static term that appears due to the cosine squared. This will ultimately be absorbed into the first term of Equation 42. With this definition of I_O^2 we can write the convolution integral from the third term of Equation 42 as

$$bI_O^2 * D = 2bI_1 I_2 * D + N_{osc}^{(2)} \exp \left[2i\vec{q} \cdot \vec{r} \right] + c.c. \qquad (47)$$

with

$$N_{osc}^{(2)} = \left[2bI_1 I_2 e^{2i(\Delta \phi - \delta t)} \right] * D. \qquad (48)$$

We may now rewrite Equation 42 as

$$NE = N_{stat} E + \left[N_{osc}^{(1)} \exp (i\vec{q} \cdot \vec{r}) + c.c. \right] E + \left[N_{osc}^{(2)} \exp (2i\vec{q} \cdot \vec{r}) + c.c. \right] E \qquad (49)$$

with

$$N_{stat} = \left(aI_S + bI_S^2 + 2bI_1 I_2 \right) * D. \qquad (50)$$

Spatial Phase Matching Considerations.

We must now distribute the oscillating terms across the total electric field. In Equation 49, both the second and third terms will result in four new terms plus their complex conjugates. Our goal here is to derive a system of ordinary differential equations governing A_1 and A_2 and determine which of these new terms will spatially phase match along the z-axis and experience exponential character. Assuming a degenerate frequency interaction, i.e. neglecting the ω terms, and recalling $\vec{q} = \vec{k_1} - \vec{k_2}$,

31

we can define the second term of Equation 49 as

$$
\begin{aligned}
\left[N_{osc}^{(1)}e^{i\vec{q}\cdot\vec{r}} + c.c.\right]\left[A_1 e^{i\left(\vec{k_1}\cdot\vec{r}\right)} + A_2 e^{i\left(\vec{k_2}\cdot\vec{r}\right)} + c.c.\right] &= N_{osc}^{(1)}A_1 e^{i\left(2\vec{k_1}-\vec{k_2}\right)\cdot\vec{r}} \\
&+ N_{osc}^{(1)}A_2 e^{i\vec{k_1}\cdot\vec{r}} + N_{osc}^{(1)*}A_1 e^{i\vec{k_2}\cdot\vec{r}} + N_{osc}^{(1)*}A_2 e^{i\left(2\vec{k_2}-\vec{k_1}\right)\cdot\vec{r}} + c.c.
\end{aligned}
\tag{51}
$$

A similar approach can be taken with respect to the third term such that

$$
\begin{aligned}
\left[N_{osc}^{(2)}e^{2i\vec{q}\cdot\vec{r}} + c.c.\right]\left[A_1 e^{i\left(\vec{k_1}\cdot\vec{r}\right)} + A_2 e^{i\left(\vec{k_2}\cdot\vec{r}\right)} + c.c.\right] &= N_{osc}^{(2)}A_1 e^{i\left(3\vec{k_1}-2\vec{k_2}\right)\cdot\vec{r}} \\
&+ N_{osc}^{(2)}A_2 e^{i\left(2\vec{k_1}-\vec{k_2}\right)\cdot\vec{r}} + N_{osc}^{(2)*}A_1 e^{i\left(2\vec{k_2}-\vec{k_1}\right)\cdot\vec{r}} \\
&+ N_{osc}^{(2)*}A_2 e^{i\left(3\vec{k_2}-2\vec{k_1}\right)\cdot\vec{r}} + c.c.
\end{aligned}
\tag{52}
$$

Substitution of Equations 51 and 52 into 49 and then ultimately back into Equation 40 resolves our coupled amplitude equations. Regardless of geometery, consider the field traveling in the k_2. Neglecting linear absorption and diffraction from Equation 40, we have

$$
\begin{aligned}
\frac{1}{\sigma_{NL}}\frac{d}{dz}A_2 e^{i\vec{k_2}\cdot\vec{r}} &= N_{stat}E + N_{osc}^{(1)}A_1 e^{i(2\vec{k_1}-\vec{k_2})\cdot\vec{r}} + N_{osc}^{(1)}A_2 e^{i\vec{k_1}\cdot\vec{r}} + N_{osc}^{(1)*}A_1 e^{i\vec{k_2}\cdot\vec{r}} \\
&+ N_{osc}^{(1)*}A_2 e^{i(2\vec{k_2}-\vec{k_1})\cdot\vec{r}} + N_{osc}^{(2)}A_1 e^{i(3\vec{k_1}-2\vec{k_2})\cdot\vec{r}} + N_{osc}^{(2)}A_2 e^{i(2\vec{k_1}-\vec{k_2})\cdot\vec{r}} \\
&+ N_{osc}^{(2)*}A_1 e^{i(2\vec{k_2}-\vec{k_1})\cdot\vec{r}} + N_{osc}^{(2)*}A_2 e^{i(3\vec{k_2}-2\vec{k_1})\cdot\vec{r}}.
\end{aligned}
\tag{53}
$$

Dividing the exponential on the left hand side provides the amplitude equation for A_2 such that

$$
\begin{aligned}
\frac{1}{\sigma_{NL}}\frac{dA_2}{dz} &= N_{stat}A_2 + N_{osc}^{(1)*}A_1 + N_{osc}^{(1)}A_2 e^{i\vec{q}\cdot\vec{r}} + \left[N_{osc}^{(1)*}A_2 + N_{osc}^{(2)*}A_1\right]e^{-i\vec{q}\cdot\vec{r}} \\
&+ \left[N_{osc}^{(1)}A_1 + N_{osc}^{(2)}A_2\right]e^{i2\vec{q}\cdot\vec{r}} + N_{osc}^{(2)*}A_2 e^{-i2\vec{q}\cdot\vec{r}} + N_{osc}^{(2)}A_1 e^{i3\vec{q}\cdot\vec{r}}.
\end{aligned}
\tag{54}
$$

There first two terms on the right hand side are automatically phase matched and will be significant regardless of co- or counter-propagation geometry. The remaining

terms maintain a dependence on $\vec{q}$ in the spatial phase. Generally, these terms are neglected as they will be insignificant relative to the automatically phase matched terms for cases where $\vec{q}$ has any appreciable value. Consider counter-propagating fields where $\vec{q}$ is projected primarily along the axis of propagation (Figure 5). In this case, only the automatically phase matched terms survive. The magnitude of $\vec{q}$ will be approximately $2k_0$ for shallow angles of incidence and greater than k_0 for all other angles less than 90 degrees. The result is a derivation consistent with established theory for S/XPM-driven, degenerate frequency TBC [15]. Combining all nonlinear contributions from population redistribution and $\chi_{(3)}$ along with linear absorption, Equation 40 can be converted to a system of coupled amplitude equations such that

$$
\frac{\mathrm{d}}{\mathrm{d}z'}\begin{bmatrix} A_1 \\ -A_2 \end{bmatrix} = \left(\hat{L} + \hat{N} \right) \begin{bmatrix} A_1 \\ A_2 \end{bmatrix}.
\tag{55}
$$

The linear operator, $\hat{L}$, which captures transverse diffraction and has the form

$$
\hat{L} = \begin{bmatrix} i\frac{\nabla_\perp^2}{2k_0} & 0 \\ 0 & i\frac{\nabla_\perp^2}{2k_0} \end{bmatrix}.
\tag{56}
$$

The nonlinear operator, $\hat{N}$, governs linear and nonlinear absorption, refraction, and coupling which takes the form

$$
\hat{N} = \begin{bmatrix} \sigma_{NL}N_{stat} - \frac{\alpha_0}{2} + \chi_{(3)}\left(I_1 + 2I_2\right) & \sigma_{NL}N_{osc}^{(1)} \\ \sigma_{NL}N_{osc}^{(1)*} & \sigma_{NL}N_{stat} - \frac{\alpha_0}{2} + \chi_{(3)}\left(I_2 + 2I_1\right) \end{bmatrix}
\tag{57}
$$

with the off-diagonal terms driving energy transfer.

Coupled Irradiance and Phase Equations.

The final step will be to convert the amplitude equation into a coupled intensity (or more accurately, irradiance) and phase equations to resolve the unique features of TBC in resonant Kerr media. This will further illustrate the inherent differences between co- and counter-propagating geometries.

Utilizing Equations 5 and 19 and expanding σ_{NL} and $\chi_{(3)}$, the coupled amplitude equation for A_2 in a counter-propagating geometry may be rewritten as

$$
-\frac{d\sqrt{I_2}}{dz}e^{i\phi_2} - i\sqrt{I_2}e^{i\phi_2}\frac{d\phi_2}{dz} =
$$
$$
\left[\left(i\frac{2\pi\sigma_{ref}}{\lambda_0} - \frac{\sigma_{abs}}{2}\right)N_{stat} - \frac{\alpha_0}{2} + \left(i\frac{2\pi}{\lambda}\gamma - \frac{\beta}{2}\right)(I_2 + 2I_1)\right]\sqrt{I_2}e^{i\phi_2} \quad (58)
$$
$$
+ \left(i\frac{2\pi\sigma_{ref}}{\lambda_0} - \frac{\sigma_{abs}}{2}\right)N_{osc}^{(1)*}\sqrt{I_1}e^{i\phi_1}.
$$

Dividing the exponential from the left hand side gives

$$
-\frac{d\sqrt{I_2}}{dz} - i\sqrt{I_2}\frac{d\phi_2}{dz} =
$$
$$
\left[\left(i\frac{2\pi\sigma_{ref}}{\lambda_0} - \frac{\sigma_{abs}}{2}\right)N_{stat} - \frac{\alpha_0}{2} + \left(i\frac{2\pi}{\lambda}\gamma - \frac{\beta}{2}\right)(I_2 + 2I_1)\right]\sqrt{I_2} \quad (59)
$$
$$
+ \left(i\frac{2\pi\sigma_{ref}}{\lambda_0} - \frac{\sigma_{abs}}{2}\right)N_{osc}^{(1)*}\sqrt{I_1}e^{i(\phi_1-\phi_2)}.
$$

In order to separate this equaiton into real and imaginary components, we define

$$
N_{osc}^{(1)*}e^{i(\phi_1-\phi_2)} = \left|N_{osc}^{(1)}\right|e^{i(\Delta\phi-\phi_{Nosc})}
$$
$$
= \left|N_{osc}^{(1)}\right|\cos\left(\Delta\phi - \phi_{Nosc}\right) + \left|N_{osc}^{(1)}\right|i\sin\left(\Delta\phi - \phi_{Nosc}\right) \quad (60)
$$

where the magnitude and phase of $N_{osc}^{(1)}$ is defined by Equation 45. Note that the phase difference, $\Delta\phi - \phi_{Nosc}$, represents the physical shift between the holographic

34

grating and interference pattern. The square root may also be addressed with

$$\frac{dI}{dz} = 2\sqrt{I}\frac{d\sqrt{I}}{dz}. \tag{61}$$

With these definitions, Equation 59 can now be split into two equations,

$$
\begin{aligned}
-\frac{dI_2}{dz} &= -\left[\sigma_{abs}N_{stat} + \alpha_0 + \beta\left(I_2 + 2I_1\right)\right]I_2 \\
&- \left[\sigma_{abs}\left|N_{osc}^{(1)}\right|\cos\left(\Delta\phi - \phi_{N_{osc}}\right) + \frac{4\pi}{\lambda_0}\sigma_{ref}\left|N_{osc}^{(1)}\right|\sin\left(\Delta\phi - \phi_{N_{osc}}\right)\right]\sqrt{I_1 I_2}
\end{aligned}
\tag{62}
$$

and

$$
\begin{aligned}
-\frac{d\phi_2}{dz} &= \frac{2\pi\sigma_{ref}}{\lambda_0}N_{stat} + \frac{2\pi}{\lambda}\gamma\left(I_2 + 2I_1\right) \\
&+ \left[\frac{2\pi}{\lambda_0}\sigma_{ref}\left|N_{osc}^{(1)}\right|\cos\left(\Delta\phi - \phi_{N_{osc}}\right) - \frac{\sigma_{abs}}{2}\left|N_{osc}^{(1)}\right|\sin\left(\Delta\phi - \phi_{N_{osc}}\right)\right]\frac{\sqrt{I_1}}{\sqrt{I_2}}
\end{aligned}
\tag{63}
$$

one governing irradiance and one for phase, respectively. Recalling the definition for $N_{osc}^{(1)}$ from Equation 45 resolves the troubling irradiance ratio in the phase equation and reconciles the derivation with [8]. An nearly identical set of equations can be written for I_1 with the exception of the complex conjugate of the coupling term in the nonlinear operator, i.e.

$$
\begin{aligned}
N_{osc}^{(1)}e^{-i(\phi_1 - \phi_2)} &= \left|N_{osc}^{(1)}\right|e^{-i(\Delta\phi - \phi_{N_{osc}})} \\
&= \left|N_{osc}^{(1)}\right|\cos\left(\Delta\phi - \phi_{N_{osc}}\right) - \left|N_{osc}^{(1)}\right|i\sin\left(\Delta\phi - \phi_{N_{osc}}\right).
\end{aligned}
\tag{64}
$$

The opposite sign in the imaginary part leads to one way energy transfer and results in the set of irradiance and phase equations,

$$
\begin{aligned}
\frac{dI_1}{dz} &= -\left[\sigma_{abs}N_{stat} + \alpha_0 + \beta\left(I_1 + 2I_2\right)\right]I_1 \\
&- \left[\sigma_{abs}\left|N_{osc}^{(1)}\right|\cos\left(\Delta\phi - \phi_{N_{osc}}\right) - \frac{4\pi}{\lambda_0}\sigma_{ref}\left|N_{osc}^{(1)}\right|\sin\left(\Delta\phi - \phi_{N_{osc}}\right)\right]\sqrt{I_1 I_2}
\end{aligned}
\tag{65}
$$

and

$$-\frac{d\phi_1}{dz} = \frac{2\pi\sigma_{ref}}{\lambda_0} N_{stat} + \frac{2\pi}{\lambda}\gamma \left(I_1 + 2I_2\right)$$
$$+ \left[\frac{2\pi}{\lambda_0}\sigma_{ref}\left|N_{osc}^{(1)}\right|\cos\left(\Delta\phi - \phi_{N_{osc}}\right) - \frac{\sigma_{abs}}{2}\left|N_{osc}^{(1)}\right|\sin\left(\Delta\phi - \phi_{N_{osc}}\right)\right]\frac{\sqrt{I_2}}{\sqrt{I_1}}. \tag{66}$$

The direction of energy transfer will then be dependent upon the sign of σ_{ref} and the argument of the sine terms in Equations 62 and 65. Additionally, if there is not physical shift between the holographic grating and the interference pattern, these sine terms go to zero and coupling does not occur.

III. Methodology

With the theoretical derivations on firm ground, this chapter will focus on the experimental techniques and numerical recipes utilized for validation. Experimentation, theory, and simulation are required for rigorous understanding. Upon consensus, the numerical model may be used for prediction and manipulation for desired application.

3.1   Numerical Modeling

One of the primary objectives of this dissertation is to develop a rigorous numerical recipe to study the S/XPM-mediated TBC. A comprehensive numerical simulation will allow for parameter exploration and optimization for desired effects, namely energy transfer and coherent amplification. First, we must define the parameter space in question and then correlate these inputs to the desired effects. Certainly the nonlinear parameters of the medium are critical. 1PA and 2PA coefficients, excited state and carrier contributions must be quantified and related to real materials. Experimental parameters are also important such as delay time, chirp structure, and intensity ratio. Our primary desired effect will be the gain coefficient for energy transfer but also the qualitative reconstruction of holographic fields will be considered.

To illustrate how self-action effects the spatial shape of the field, diffraction must be considered. This additional complication requires a Strang split step technique that separates the linear (diffraction) from the nonlinear operator in

$$\frac{\mathrm{d}}{\mathrm{d}z'} \begin{bmatrix} A_1 \\ -A_2 \end{bmatrix} = \left(\hat{L} + \hat{N} \right) \begin{bmatrix} A_1 \\ A_2 \end{bmatrix}. \tag{67}$$

[36]. Strang splitting reduces the order of error but comes with some limited computational cost. Each z slice must be further discretized into a half linear step followed

by a full nonlinear step and a second half linear step. Because of the looping strategy, half steps need only be applied to the first and last longitudinal steps. That is, the intermediate half steps can be combined. The linear operator is then solved using spectral techniques such Fourier or Hankel transforms.

Because of the counter-propagation geometry requires an iterative algorithm [44], a full rectilinear approach using fast Fourier transforms is computationally inconvenient. Instead, a radial numerical propagation operator is employed following the procedure outlined by Ref. [20]. By utilizing the Hankel transform formalism, the electric fields may be defined as vectors rather than a two-dimensional matrices thus dramatically eliminating the number of data points in memory and calculations in both the linear and nonlinear operators by orders of magnitude. The Hankel approach is mathematically and numerically equivalent.

The first step is to discretize the time, radial, and longitudinal thickness parameters. Time and longitude coordinates are evenly space according the total number of steps desired in each dimension. However, the Hankel transform algorithm requires sampling along the Bessel zeros of order zero as defined by [20]. This insures that the sampling will not be evenly spaced. This must be considered when spatially integrating fluence (J/cm^2) data in to total energy (J). Fortunately, Matlab's embedded trapezoidal numerical integration (trapz) command allows for this non-even sampling. Once the Hankel transfer functions are calculated, the radial points are defined for the entirety of the simulation. That is, unlike certain Fourier algorithms, the spatial sampling never changes. This is both good and bad. For example, it simplifies the propagation operators but makes far field propagation difficult. This will become apparent in the holographic transfer simulations shown in Chapter 5.

With the radial, temporal, longitudinal coordinates defined, the next step is to define the electric fields. Because the experimental data is an apertured plane wave

(APW) input, the focal plane will have a characteristic Airy disk pattern. This can be calculated using the procedure outlined in Ref. [4]. This calculation involves solving a series expansion of Bessel functions until a predefined tolerance is achieved. The result is a nearly analytical solution to the total APW field at the focal plane. The temporal pulse utilizes a Gaussian profile such that

$$A_t = A_0 \exp{-\frac{(t - \Delta t)^2}{\tau_L^2}} \tag{68}$$

where τ_L is the pulse width of the laser and ΔT is the relive time shift between pulses. Note that 68 is applied to the field and not irradiance. The temporal profile (1 x time steps) and radial profile (radial steps x 1) vectors form the field matrix product (radial steps x time steps). The field amplitude is then scaled to the square root of peak irradiance according to the analytical irradiance-fluence-energy relationship using

$$F_0 = \frac{\pi E}{4*\lambda^2 N^2}, \quad I_0 = \frac{F_0}{\sqrt{\pi}\tau_L} \tag{69}$$

where E is the total beam energy (J) and N is the optical system F-number. Regardless of amplitude input (energy or fleunce), a multiplier can be calculated to convert to irradiance.

A three dimensional matrix (radial step x longitudinal steps x temporal steps) for N_stat and N_osc are then initialized for all zeros. If saturation is to be consider, a ground state population matrix, N_0, of the same size is also initialized with uniform particle density (or concentration).

Next, the split step iterative loops are started as illustrated in 8. The first time step of the forward propagating field is sent through each longitudinal step utilizing the split step formalism. At each z-step, the populations of N_{stat} and N_{osc} are calculated
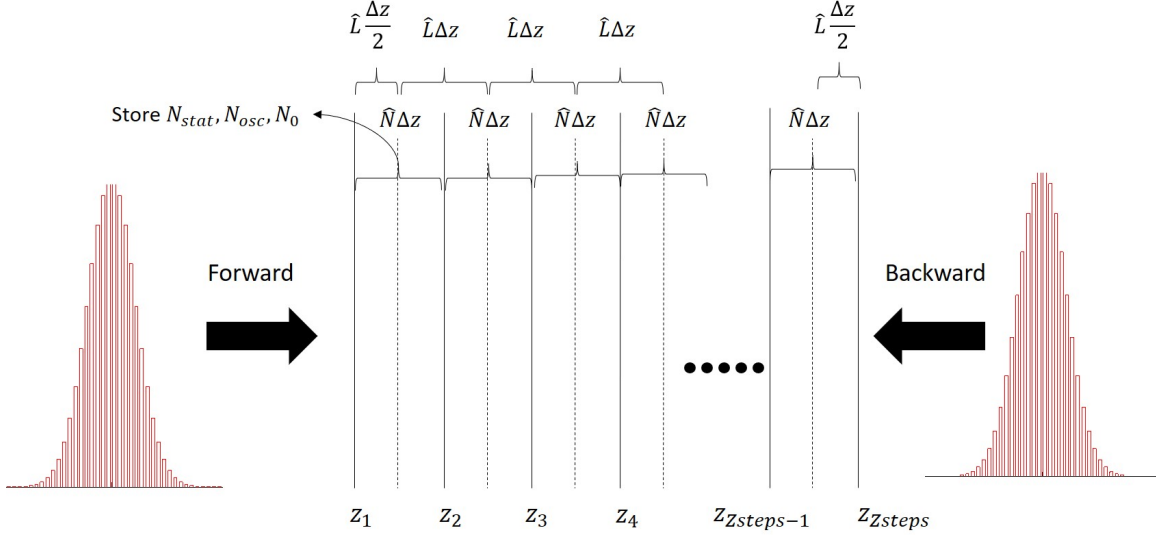
Figure 8. Discretization of temporal pulse and sample spatial dimension. For each longitudinal step, the linear operator is broken into two half steps as outlined by the Strang splitting formalism. The nonlinear operator is solved for the full step using the field calculated by the first half step. The temporal components are solved using a forward Euler recipe and the population information is stored for initial conditions of subsequent time steps.

for the next step according to the forward Euler method such that

$$N_{t+1} = \frac{f[I(t)]\Delta t + N_t}{1 + \Delta t/\tau}. \tag{70}$$

Note that $N_o sc$ is complex valued where the phase holds the grating delay relative to the interference pattern. For saturation, mass conservation is controlled by subtracting $N_s tat$ and $|N_o sc|$ from N_0. With the populations calculated, the nonlinear operator is applied using a fourth order Runge-Kutta (RK4) numerical recipe for the full longitudinal step which determines the value of the field for the next z step. This process is repeated until the first time step of the forward propagating field reaches the rear surface. At each z step the field value is stored and used for the initial conditions in the backward propagation. The first time step of the counter-propagating field is then sent backward through the medium using the same set of operations not-

ing the the indexing of the population terms are reversed. This is the first iteration. A conditional statement is then applied to determine if the results from both propagations are consistent. If not, the same time step is repeated through both forward and backward propagation until this condition is met. Only then will the next time step start using the new populations as initial conditions. This process is repeated until all time steps are completed.

For co-propagation or single beam embodiments, the iterative method is not necessary and that part of the code is turned off. Additionally for rapid evaluation, diffraction can be ignored as well and a single radial point can be used approximating a plane wave spatial distribution. For the Fresnel coupling case, the counter-propagating field is derived from the forward-propagating field at the last surface according the Fresnel equation and refractive index of the material.

3.2 Experimental

This section will discuss how all these phenomena express themselves experimentally. In 2010, Christodoulides et. al. provided a review of many of these effects [9]. In the introduction of that work, the author states, "Nonlinear optics is primarily an experimental discipline!". It is only through direct observations that we are able to make assignments of the unique and diverse physical mechanisms.

Z-Scan is a nearly universally accepted experimental apparatus for measuring Kerr nonlinearities [42]. With open and closed aperture embodiments, this experiment can quantify both the real and imaginary contributions from $\chi_{(3)}$. The beam energy is kept constant while the sample is translated through a well-characterized focus (along the optical z-axis for which the experiment is aptly named). Unfortunately, this experimental geometry is not amenable to measurements of the coherent backscatter of interest in this work especially in the case of Fresnel coupling. Instead, a fixed sample

location is employed and the beam energy is varied allowing for a more reliable optical alignment to the backscatter energy probe. This version of nonlinear measurement is referred to as I-Scan, or Irradiance Scan. Much of the experimental methodology presented here has been previously published [19, 48, 50, 47]. Another advantage of I-Scan is it allows the focal plane of the beam to be re-imaged providing a much richer objective function for numerical analysis.

For all experimental work, a frequency doubled nsec pulsed Nd:YAG laser was used (532 nm). This laser system was equipped with a seed laser for single longitudinal mode operation to increase the coherence length. In previous work [48, 49], this laser was used to pump a dye laser to generate wavelengths in the near infrared (700 and 785 nm). The pulse width was experimentally measured at 3.6 nsec (1/eHW) using an oscilloscope and a GaAs photodiode (6 and 10 GHz bandwidth respectively).

Spatially Resolved I-Scan and Fresnel Coupling.

The utility of I-Scan for quantifying third order nonlinear parameters was also addressed in Ref. [47]. This embodiment includes a third energy probe to collect the coherent backscatter necessary for this work as shown in Figure 9. The laser light is conditioned by flood loading a small aperture (2 mm) in the near field of the laser output. The beam then forms an Airy pattern in the far field of this aperture after approximately 8 meters of free space propagation. While this sacrifices a significant portion of the laser energy, the purpose is to provide a smooth, flat field.

The far field Airy pattern has a predictable amplitude and more importantly, a flat phase distribution. The beam is then collimated and expanded with a 2x telescope and this Airy beam is then flood loaded onto a second 5 mm aperture providing a flat top amplitude. A portion of the beam is split and sent to the sampling arm where the energy and pulse widths are quantified. The remaining light is sent
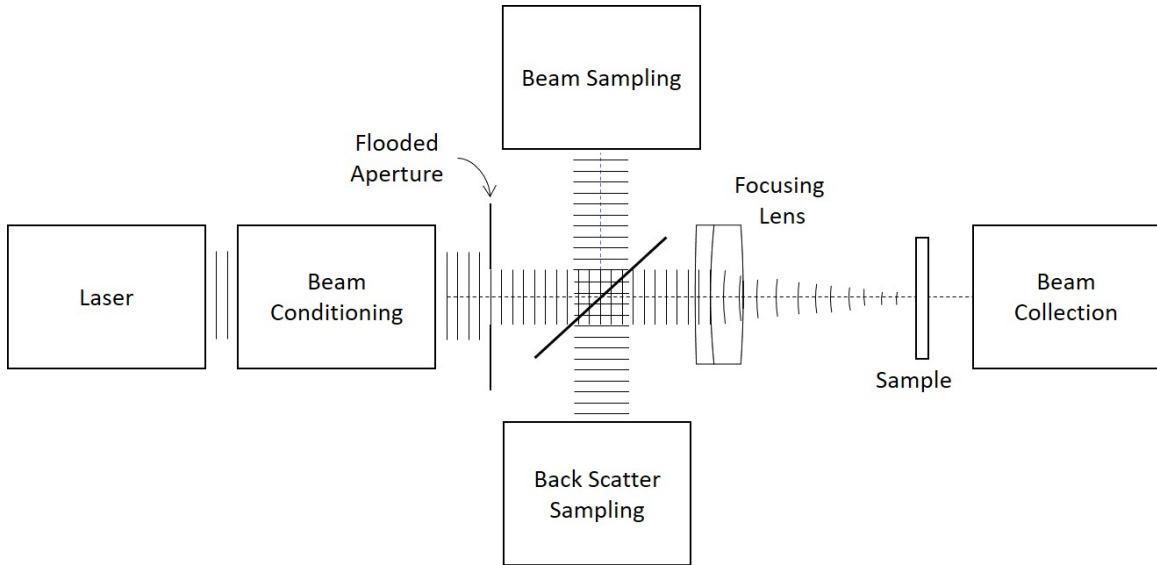
Figure 9. Spatially resolved nonlinear beam transmission experimental setup, or I-Scan. A laser is conditioned to deliver a flat field. A portion of this beam is sampled to measured incident beam parameters then sent through a focusing lens where the sample is placed at the focal plane. Backscattered light is collected by the focusing element and sent to a separate energy meter using the sampling optic for the incident beam. Light transmitted is captured by the beam collection optics.

through the focusing lens (200 mm achromatic doublet) and finally meets the sample. The transmitted bean is collected by a long working distance Mitutoyo microscope objection (20x) as shown in Figure 10. A series of neutral density filters are placed directly behind the objective to attenuate the beam to an appropriate level for the collection instruments. The beam is again split and a portion is directed to a silicon energy probe (Laser Probe Rj-735, not shown) and a second portion is refocused onto a Spiricon beam profiling CCD. The objective, filters, silicon meter, and CCD are mounted to a single breadboard with optical z-axis translation for focusing. This breadboard assembly is referred to as the calibrated fluence profiler, or CFP. Care is taken to position the sample such that the laser focus is placed on its rear surface. This is achieved by first positioning the CFP such that the object plane of the objective is confocal with the focusing lens, i.e. the laser focal plane is imaged on the CCD. The beam is then blocked and an incoherent light source (green LED) is injected into the

beamsplitter to illuminate the sample.
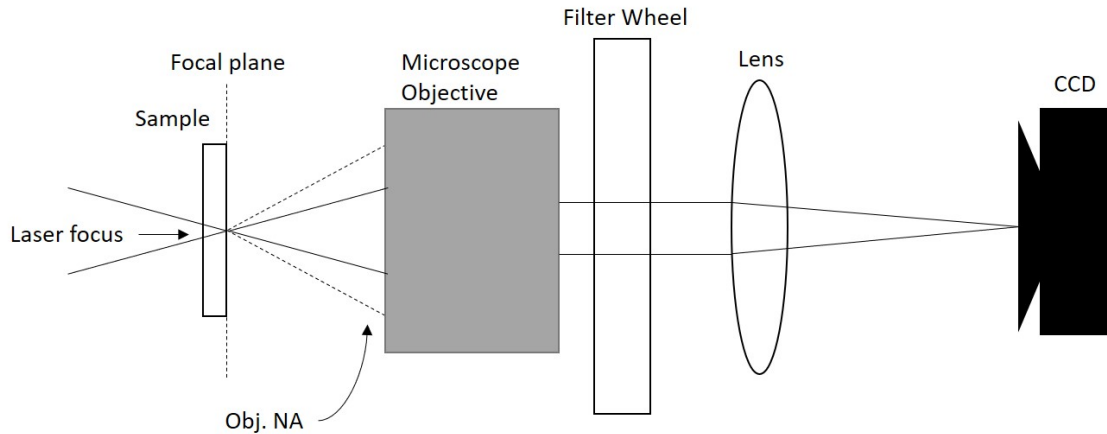
Figure 10. The beam collection optics or the calibrated fluence profiler (CFP). A long working distance, infinite conjugate microscope objective is used along with a 200 mm achromatic doublet to magnify and an image the focal plane of the laser onto a beam profiling camera (Spiricon). Filters are utilized in the collimated space to attenuate the beam within the operational sensitivity of the CCD.

The sample is then independently translated along the optical axis until its rear surface is in focus. Special care is also taken to insure calibration of each component. For example, the magnification of the objective is measured with a bar target and each meter, filter, and splitting factor is measured versus air to provide accurate absolute energy measurements. With this information the pixel responsivity is then calculated to provide an absolute fluence map of the focal plane. The image of the Airy disk focus shown in 11 is an actual laser pulse image collected by this apparatus and is effectively diffraction limited provided an analytical function for calibration purposes. Also shown is the numerical processing of the transmitted beam profiles to deliver the peak transmitted fluence, F_0 and the total encircled energy, $E(r)$. In general, The diffraction limited operation allows for radial analysis providing a critical objective function for nonlinear beam propagation simulations outlined in subsequent chapters.

Figure 12 shows a typical nonlinear response for E3PA media. In this example, 50
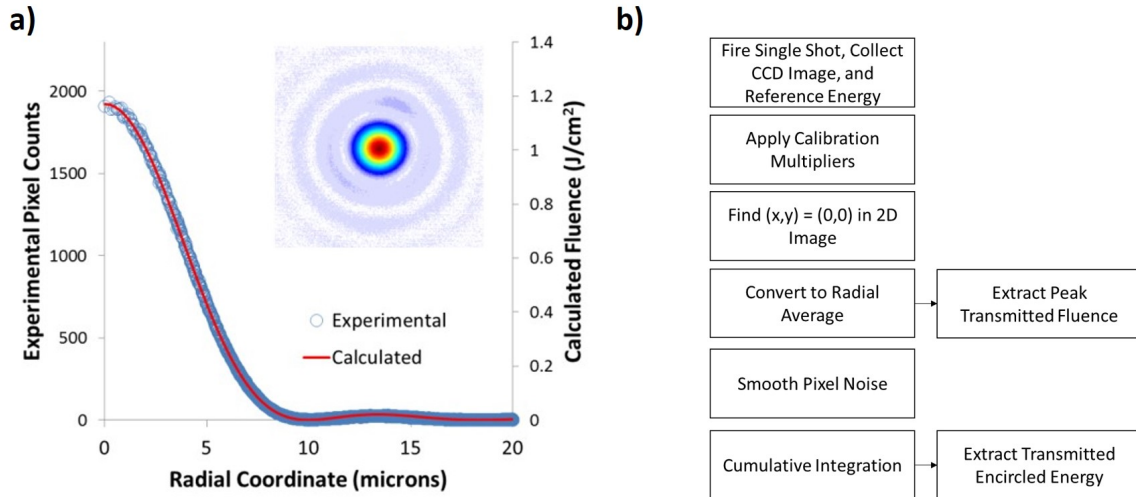
Figure 11. Instrument response and data processing flowchart for I-Scan apparatus. The experimental beam generated by the beam conditioning section is nearly diffraction limited providing an analytical objective for calibration. The radial symmetry of the apertured plane wave (APW) allows for efficient numerical analysis shown by the block diagram all performed with MATLAB real time.

mM E1BTF in solution demonstrates a strong nonlinear response in the transmitted peak fluence, F_0, above approximately 1 J/cm^2 evidenced from the inset. The spatial profiles illustrate the effect. In the linear domain, the profile is a typical Airy disk. As the incident fluence is increased, the beam is preferentially attenuated on axis due to absorption from the persistent excited state population. A radial average of the attenuated profile is shown compared to the analytical input.

To quantify Fresnel-driven TBC or Fresnel Coupling, the sample is aligned exactly normal to the laser beam k-vector to provide optimal spatial overlap both transverse, r, and longitudinal, z. The coherent backscatter, i.e. the TBC signal, is then collected by the focusing lens in the reverse direction, directed by the beamsplitter, and quantified by a silicon energy probe. Additional experiments are performed with the sample slightly tilted to spoil this effect to monitor the single beam transmission which will be used to baseline the nonlinear parameters of the sample. As an example, Figure 13 illustrates the strong Fresnel coupling observed in E1BTF measured
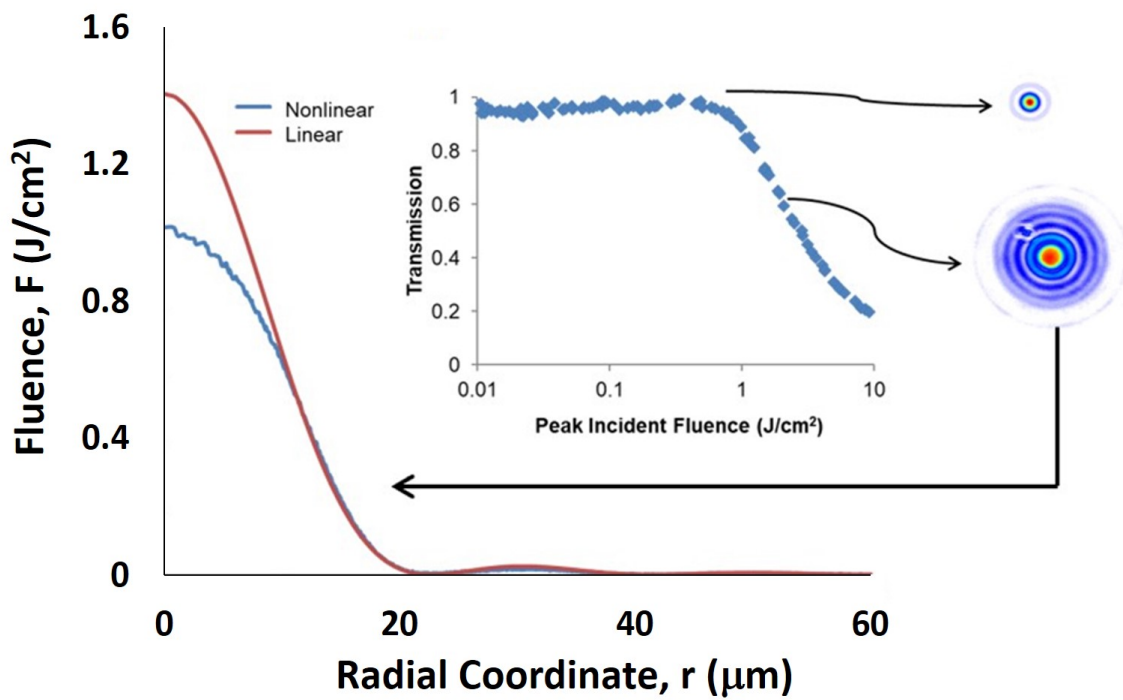
Figure 12. A typical nonlinear transmission result. The example shown here is a nonlinear dye, E1BTF [40]. Strong nonlinear absorption is evidenced by the preferential reduction of energy on axis compared to the analytical Airy disk input.

I-Scan with a 785nm pump [49, 48]. Nonlinear absorption is observed in the peak fluence, F_0, and total integrated energy, E. Total energy is defined as $E(r = max)$ where the maximum r value is determined by the CCD field of view. The obvious difference between F_0 and E transmission curves is a consequence of the intensity dependent nonlinearity as energy off-axis, i.e. the Airy rings, pass through with little to no attenuation. The Fresnel Coupling signal approaches 70% including the linear specular reflections from each glass-air interface (approximately 4% from each surface). As a result, the nonlinear self-action in E1BTF in this scenario is dominated by Frensel-driven TBC and not the expected E3PA absorption.
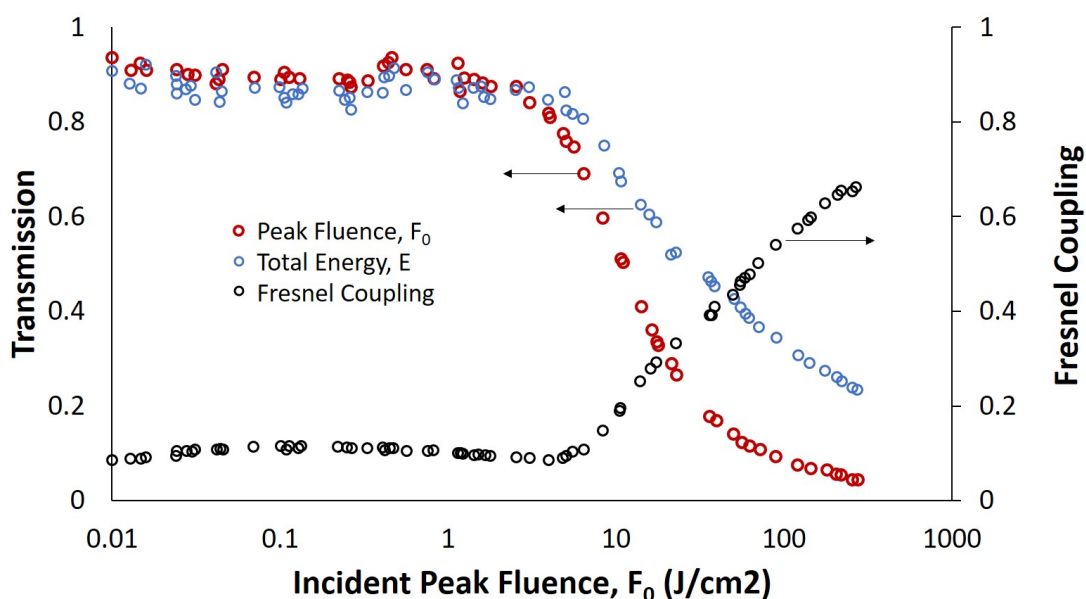
Figure 13. I-Scan results for 50mM solution of E1-BTF in THF and 2 mm cuvette. The optical geometry was set to F/40 (5mm aperture and 200 mm focal length lens) at a wavelength of 785 nm corresponding to the strong 2PA and ESA of the dye. The reduction in transmitted fluence and energy are coincident with the strong Fresnel Coupling signal. The dramatic reduction in transmission is often confused with strong ESA. In this case it is apparent that the primary source of attentuation int the foward direction is due to Fresnel-driven TBC [49].

Two Beam Counter-Propagating Experimental Setup.

For the deliberate, degenerate frequency TBC experiments performed in Ref. [49] and repeated in this work, the CFP assembly was removed and a delay line was added. The same beam conditioning procedure was used as discussed previously. The sample was angled to spoil any Fresnel driven TBC. A second set of beam splitter and focusing lens were added on the opposited side of the sample. Care was taken to insure the lenses were confocal in order to place the laser focal planes inside the nonlinear medium. One lens was mounted in a linear translation stage to account for differences in optical paths of different samples to further insure confocal alignment. A shear plate was also empolyed to determine planar wavefronts into and out of the optical system. The delay was approximately 7 nsec in total length and the probe pulse was positioned temporally in the middle providing $\pm\tau_L$ on either side. Since both fields are derived from the same source, they are degenerate in terms of frequency content. Additionally, the pump laser is seeded for single longitudinal mode output insuring a practically transform-limited frequency spectrum (approximately 500MHz in spectral bandwidth). The introduction of the temporal delay is therefore critical source for asymmetry and one-way energy transfer [56]. Additionally, one field (probe) may be attenuated relative to the second (pump) field as yet another form of asymmetry and analogous to the Fresnel coupling case where the delay is effectively zero.

The counter-propagating geometry can provide some very useful information about the nature of the TBC mechanism. As the pump pulse shifts through a weaker probe pulse in time, the direction of energy exchange will flip. The delay corresponding to this transition is called the zero-energy exchange delay. It's location indicates the TBC governing nature. If this transition occurs at zero delay, TBC is purely driven by either chirp or explicitly non-degenerate frequency inputs [13, 56]. If on the other hand, TBC is driven by nonlinear accumulation of S/XPM, the transition occurs
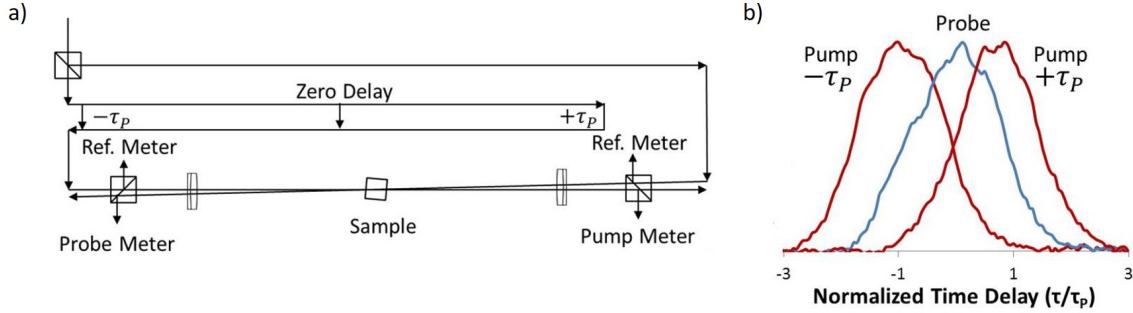
Figure 14. a) Experimental setup of counter-propagating fields with three possible fixed delays to introduce the asymmetric geometry for degenerate frequency TBC. **b)** Temporal waveforms are measured with a pulse width of 3.6 nsec (1/eHW). Note that the samples are positioned in the focal plane of confocal lenses with a slight tilt to remove any Fresnel coupling contributions to the TBC signal.

away from the zero time delay, i.e. where the pulses are exactly overlapped [15, 49]. Additionally, if energy is transfered from the lagging pulse to the leading pulse for equal energy beams, the sign of the nonlinearity is negative and vice versa.

Holographic Amplification.

In addition to energy scaling, TBC is a fundamentally holographic process which has been demonstrated at length in tranditional photorefractive media [21, 33, 38]. In order to capture the holographic nature of TBC, a second embodiment of this setup involves placing a AF1951 bar target transparency in the probe path of a confocal $4f$ imaging system configuration [5]. A CCD is placed in the image plane of the optical system as shown in Figure 15.

The bar target image captured by this CCD is shown in the right of Figure 16. The middle image is the raw probe beam spatial profile in the object plane without the bar target and is approximately 5 mm in diameter. the spatial distribution of the probe beam is lopsided due to the dye laser cavity output and the rings are a result of the flooded aperture in Figure 9. However, the contrast from the bar target transparency is easier describable. A much stronger counter-propagating pump

49
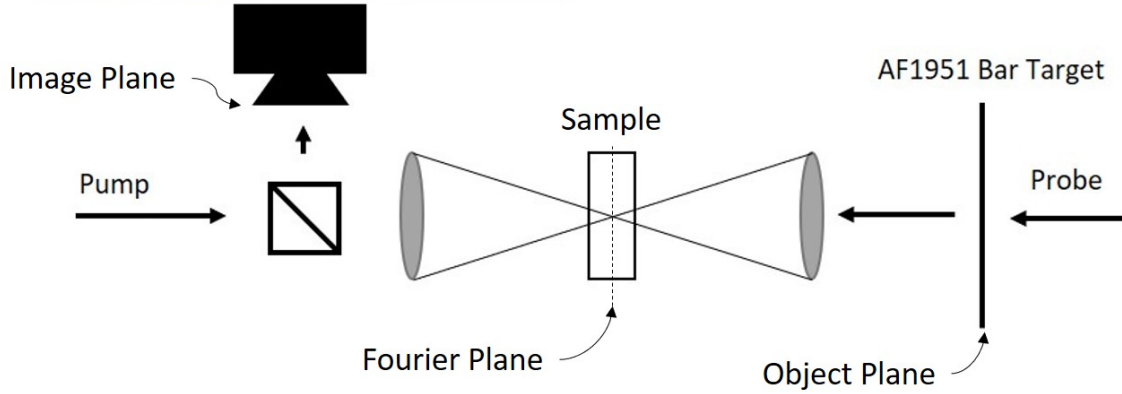
Figure 15. Experimental setup with AF1951 Bar Target re-imaged in 4f optical geometry. A weak probe beam is passed through the transparency and focused into the nonlinear media. A much stronger counter-propagating pump beam is confocally overlapped allowing for energy transfer while maintaining the spatial phase information embedded in the probe field, or coherent amplification.

beam is then aligned such that its focal plane coincides with the Fourier plane of the bar target. Energy exchange between the strong pump and weak probe maintain the spatial phase information contained in the probe field and will be discussed in subsequent sections.

Two Beam Co-Propagating Experimental Setup.

To achieve optimal energy transfer and practical implementation, a co-propagation geometry would be preferred. In fact, significant amount of the experimental effort was expended in this task. The procedure outlined in 14 was adjusted such that the pump and probe beams where both incident on the front surface of the sample. This allowed for the inclusion of the CFP breadboard for imaging.

The CFP assembly was used to align the two beam in at the focal plane of a 200mm achromat. The rear surface of the sample was then moved into focus. Following alignment, the CFP was translated backward to allow for beam separation in the field of view of the CCD. Angular separation of the beams was kept small but

Figure 16. The raw probe image is is approximately 5 mm in diameter nearly filling the CCD. The bar target is placed in the beam at the object plane of the $4f$ imaging system. The CCD focal plane is then placed in the image plane where the Group 1 bars are in focus. The red box illustrates the approximate field of view.

finite with just enough such the beam profiles could be seen separately on the image. The incident fluence was then increased in an attempt to resolved TBC. As will be discussed in detail in Chapter 4, co-propagating TBC was never observed in both semiconductor and 2PA/E3PA media.

Spectral Measurement Using Scanning Fabry-Perot Etalon.

In order to imporve upon the spectral measurements provided by He et. al. [24], a scanning Fabry-Perot Etalon (FPE) experiment was incorporated into the optical setup. The FPE apparatus was placed into the scattered field. A shear plate was utilized to insure the linear Fresnel reflection was well collimated in this path. A 75mm lens was placed such that its focal plane was centered into the FPE cavity according the Thor labs instructions. The FPE cavity was mounted in a five axis positioner and a continuous wave, solid state laser was used as a pilot beam to align the FPE cavity for optimal performance. Shown in Figure 18, a scanning FPE operates by ramping the voltage of an intra-cavity piezoelectric transducer to shift the etalon passband. A
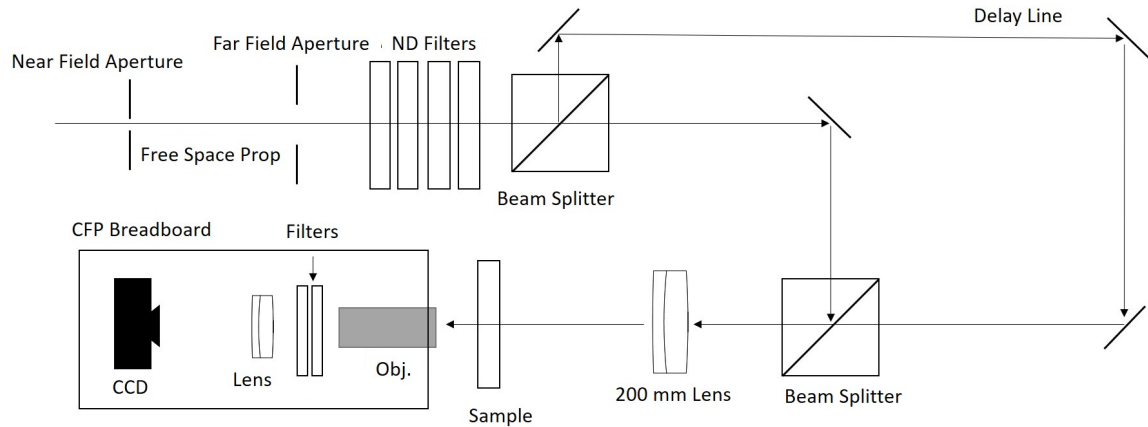
Figure 17. Experimental setup for co-propagating geometry. The pump is split into two nearly equal energy beams where one is sent into a delay line. The relative energies are controlled by placing attenuators in the respective paths as necessary. The two fields are then recombined using a second beam splitter such that the angular separation is approximately defined by the numerical aperture of the 200mm achromat or roughly 0.1 radians or 6 degrees.

Thor Labs SA200-5B model was utilized in this experiment with a cavity length of 50mm, free spectral range of 1.5GHz, and a resolution of 7.5MHz.

Special care was taken to synchronize the piezoelectric voltage ramp to the 10Hz repetition rate of the laser resulting in a signficantly slower ramp time than typically used. This in turn resulted in a noticeable but systematic drift from scan to scan. However, this low frequency drift was well below the bandwidth of the nsec laser source and therefore was neglected.

A collection aperture was placed just before the focusing lens to exclude portions of the linear Fresnel beam for alignment. Also evident in Figure 19 is spatial blooming in the coherent backscatter as the incident fluence was increased. The aperture diameter was adjusted to capture enough of this backscatter to provide sufficient signal to noise. A shear was used to insure collimation of both the linear and nonlinear signals as required for proper FPE alignment. There was no discernible difference in collimation from the two signals. Details on the spectral content of the Fresnel coupled TBC signal is addressed in the Results and Discussion section.
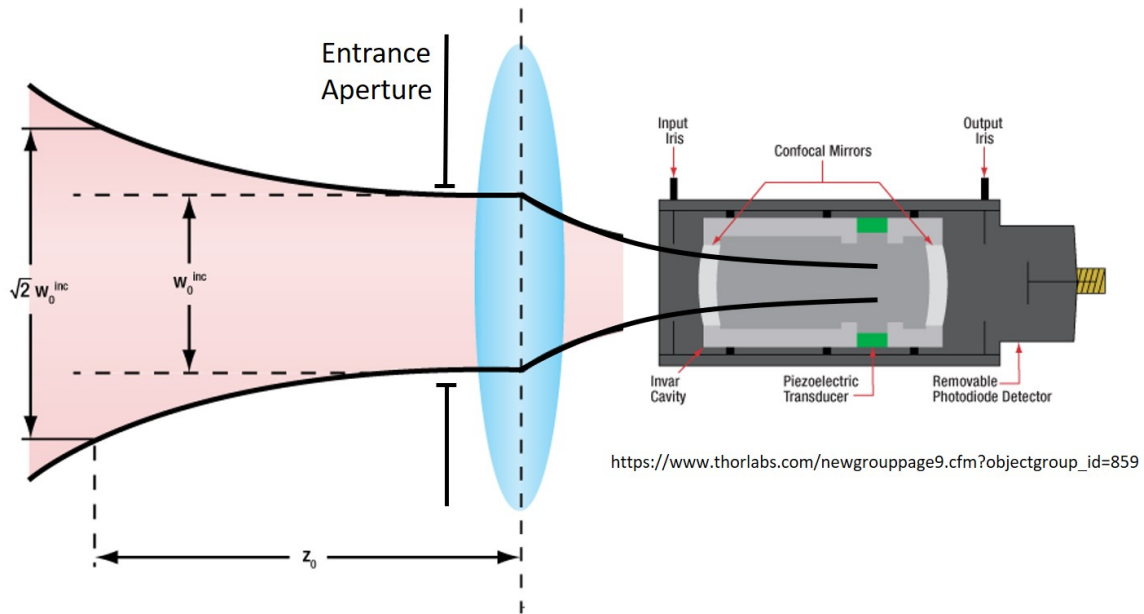
Figure 18. Alignment of scanning Fabry-Perot Etalon cavity to capture the spectral content of the scattered field. An entrance aperture was placed just prior to the focusing lens to spatially filter the signal. A special collection program was written to enable single shot acquisition at the laser repetition rate of 10Hz.
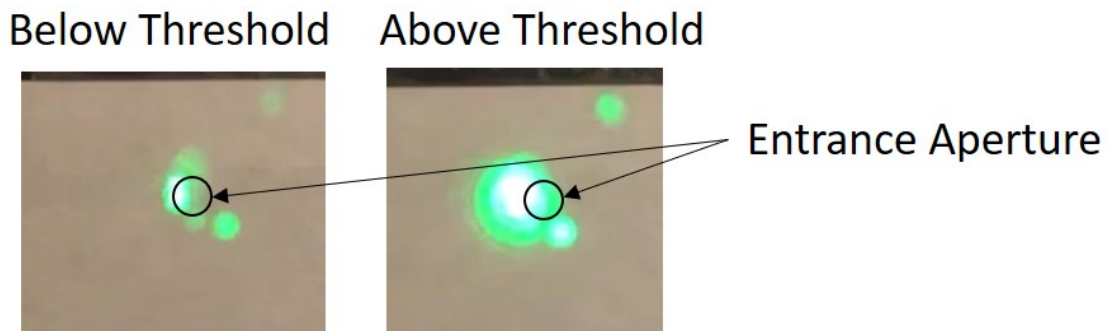
Figure 19. The entrance aperture was placed just off-center of the linear Fresnel beam for alignment to collect the bloomed backscatter signal. Both the linear and nonlinear beams were checked with a shear plate to insure collimation for accuracy.

IV. Results and Discussion

Early work focused on E1BTF solutions in the near IR (700nm and 785nm) where linear absorption is negligible [49]. This work is revisited here to the validate the numerical model specifically for the counter-propagating case where no other data exists. Additional unpublished, follow-up work with E1BTF at 532nm is now presented. At this wavelength, 2PA cross sections for E1BTF have not been quantified. However, resonant enhanced 2PA is to be expected [14] and a value is approximated through numerical fitting of I-Scan data. The numerical model is also applied at this wavelength where Fresnel coupling, co-propagating TBC, and FPE spectral measurements were performed. Material inputs are collated in Table 1 shown in the Appendix.

4.1 Fresnel Coupling

Fresnel coupling is by far the simplest to observe experimentally owing to the optimal overlap of both transverse and longitudinal spatial dimensions. Figure 24 displays the transmission plots for a solution of 0.05 mM E1BTF in THF as a function of increasing pump fluence at 532nm. The characteristic decrease in both total energy transmission and drop in peak fluence transmission are present along with the Fresnel coupled TBC signal as was the case for 785 nm. For reference, fluence transmission is the ratio of the on-axis values of the transmitted beam and the theoretical, diffraction limited peak fluence. Energy transmission is the spatially integrated fluence divided by the measured input energy. The open circles are the experimental data and the solid lines are the simulated results from the full diffraction, iterative split step numerical recipe. Exceptional agreement is achieved for both the energy and fluence transmission curves. Modest gain is observed in the simulation for the backward propagating field. However saturation takes effect in the numerical recipe

54

and the Fresnel Coupling signal begins to level out soon after threshold. Qualitatively, the transfer threshold is well predicted by this model with exponential gain following experimentally.
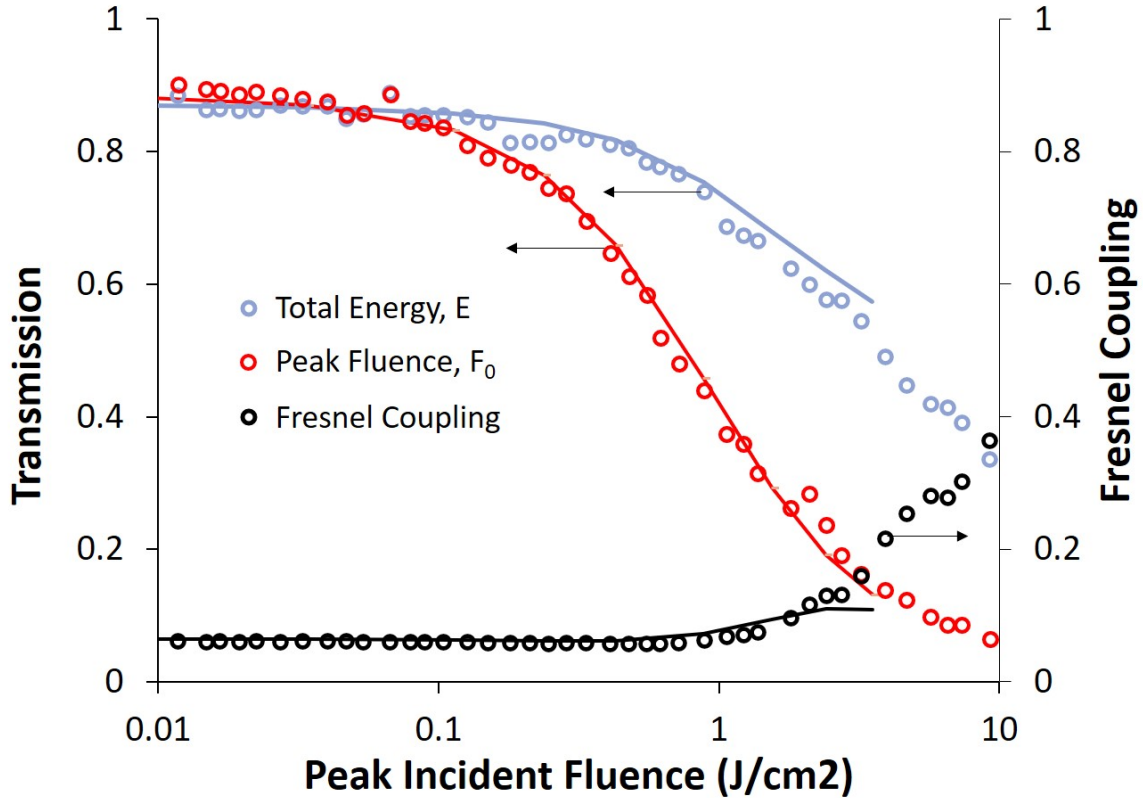
Figure 20. Experimental validation of E1BTF I-Scan results with quantified Fresnel coupled TBC compared with full diffraction simulation. There is strong agreement both in fluence profile and transmission measurements. TBC simulations match well until nonlinearity saturates.

Figure 21 is the radial profile for a pump fluence of 1.8 J/cm². The red line is the radial average of the experimental data measured at the focal plane with CFP apparatus, the dashed line is the theoretical, diffraction limited pump beam in the same location, and the black line is the simulated spatial distribution. Again, we observe strong agreement for the forward propagating field. Note that energy is expanding outside of the central lobe in the transmitted beam. This is characteristic of a negative value for nonlinear refraction and is evident that the numerical simulation

is capturing both nonlinear absorptive and refractive contributions with values of $3x10^{-17}$ cm^2 and $-1x10^{-21}$ cm^3, respectively (see Table 1). The apparent presence of nonlinear refraction is critical for driving Fresnel Coupling.
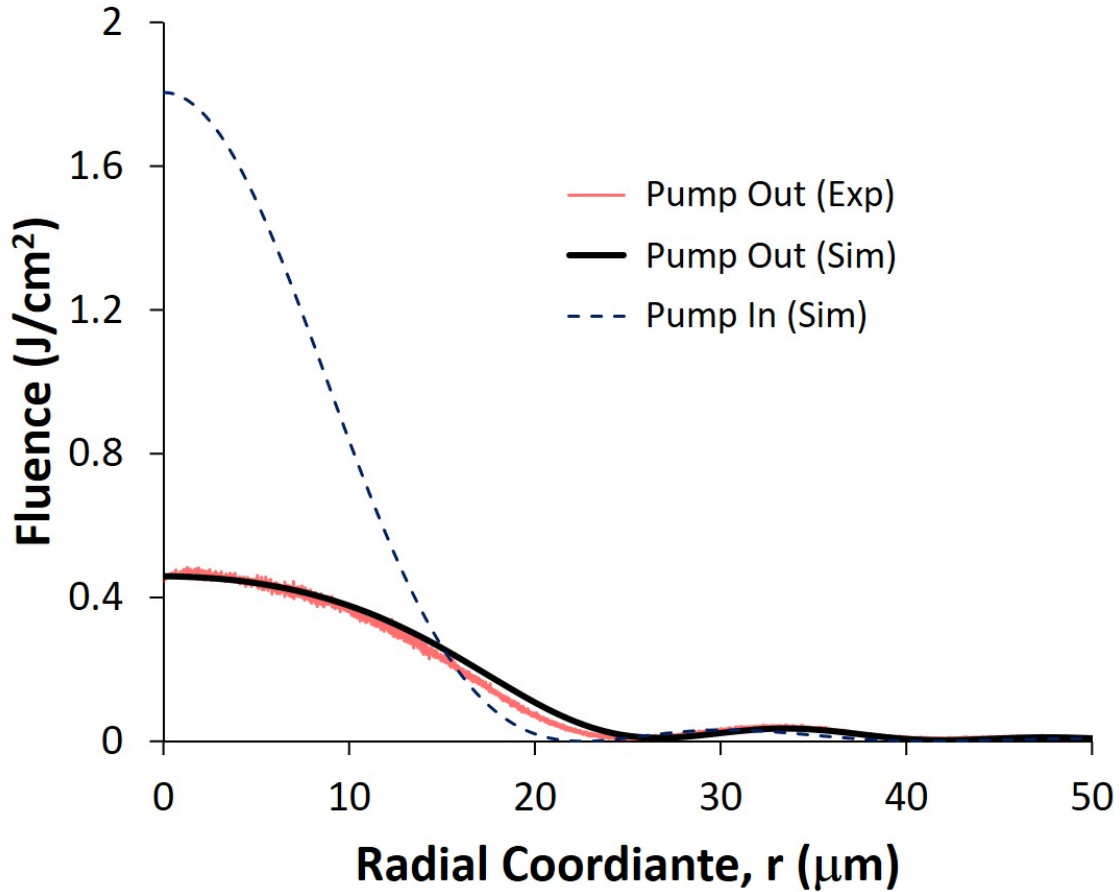
Figure 21. Simulation of spatial distribution results for E1BTF at 1.8 J/cm^2. The dashed line captures the analytical Airy disk input. The black solid line is the simulated pump output and the red solid line is the radial average of the experimental result at this fluence input.

The spatial distribution of the Fresnel Coupled output in the near field of the nonlinearity cannot be directly measured in this experimental embodiment. However, numerical simulation can predict this profile. Not that for the Fresnel signal, the output beam occurs at the front surface of the sample. Figure 22 shows the backward propagating (Fresnel Coupled TBC signal) as it exits this front surface of the sample

compared to the input which is the partially reflected pump field (approximately 4% of the pump output). Gain is accumulated preferentially near the optical axis where the pump intensity is the strongest as would be expected. This along with diffraction and nonlinear refraction generates an odd spatial distribution. However, this profile is consistent with the bloomed output in the far field.
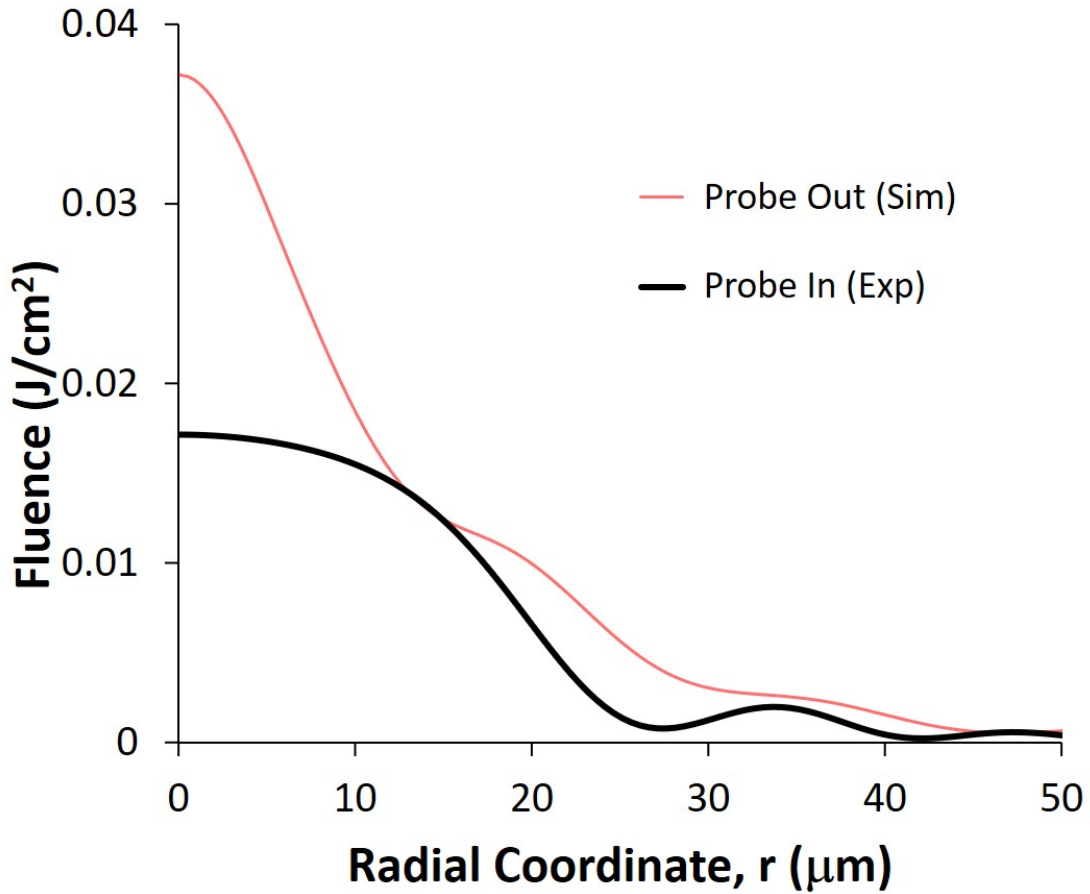
Figure 22. Simulated Fresnel coupled beam profile as it exits the sample compared to the pump incident and transmitted profiles. Since the probe beam is derived directly from the pump, the input is a the pump output multiplied by the Fresnel reflection (0.04). The gain in the probe field is apparent with preferentially near the optical axis where the pump intensity is strongest.

Another observation for E1BTF is that these results are very similar to the published results at 785nm [49] illustrating the broadband nature of degenerate TBC in this material. E1BTF was specifically engineered to work as a broadband nonlinear

absorber [40], so the presence of TBC throughout Figure 4 is not surprising. For 785 nm, linear loss is negligible and strong excite state resonance delivers both absorptive and refractive, cumulative nonlinearities leading to ideal conditions. Conversely at 532 nm, linear absorption is stronger near the ground state resonance and the excited state properties are weaker leading to the diminished coupling efficiency.
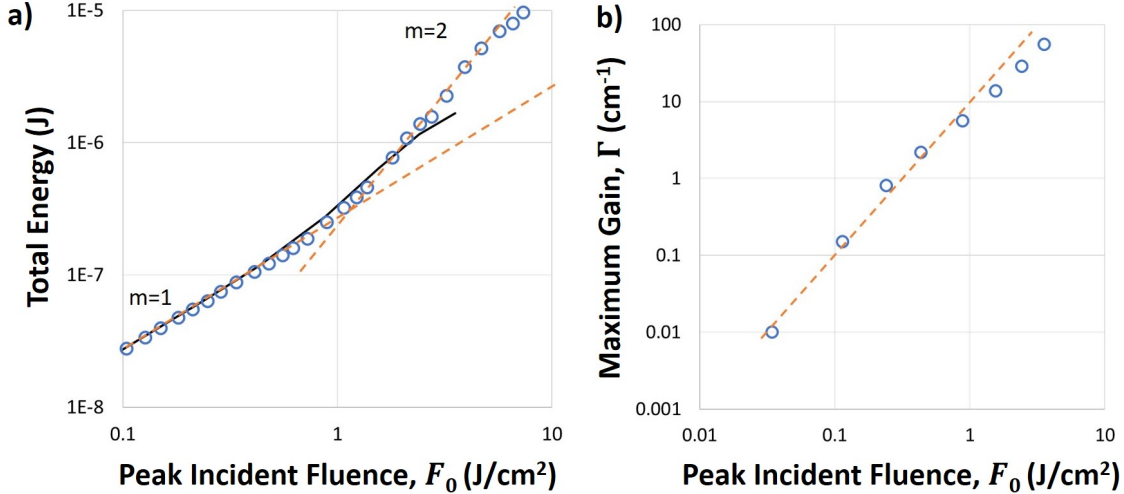
Figure 23. Experimental and full diffraction simulation results for TBC energy as a function of incident pump fluence. A clear quadratic dependence is evident in the experimental results with qualitative agreement to numerical results. Grid lines in logarithmic axes indicate a slope of two above threshold. a) Quadratic nature in total energy transfer to the probe beam and b) quadratic nature of gain coefficient.

Figure 23 illustrates the quadratic nature of both energy coupling and the gain function with respect to incident pump fluence. The left-hand side plot shows the experimental energy in the TBC signal. A clear linear regime exists followed by the nonlinear regime with a slope of two in log space. Simulation results are shown for comparison. The right-hand side plot is the calculated maximum gain and is also roughly quadratic but begins to saturate at high pump intensity. It should be noted that gain values exceed 50 cm^{-1} for these calculations placing it on the order of typical photorefractive values but with a near instantaneous response.

Simulations of a single on-axis radial point where also performed without diffrac-

tion to further resolve more of the qualitative aspects of S/XPM-driven TBC. Figure 24 pump/probe intensities as a function of longitudinal coordinate (z-axis or sample thickness) and time. The pump beam propagation is from left to right starting with a Gaussian temporal distribution. As the beam propagates, the pulse is attenuated in time consistent with the cumulative population nonlinearity. Conversely, the probe beam propagates right to left and starts with the specular reflection of the pump and experiences gain as the field approaches front surface of the sample.
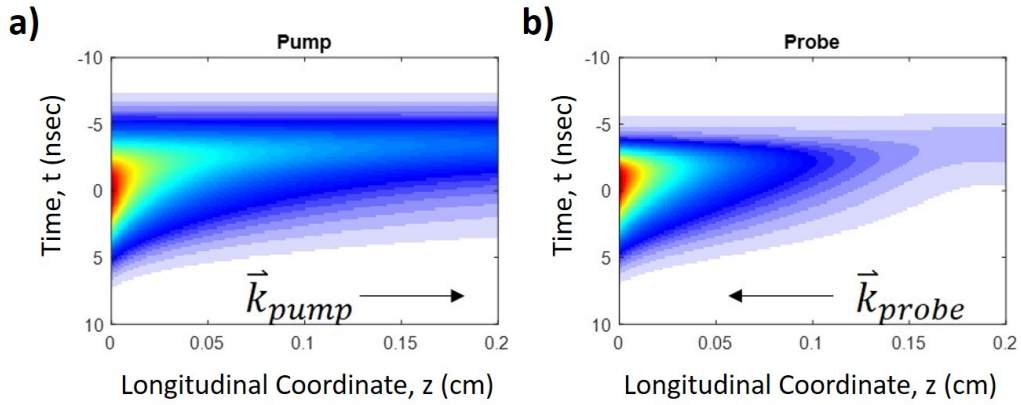
Figure 24. Summary of simulated Fresnel coupled TBC in 0.05mM E1BTF solution for on axis radial coordinate (or plane wave scenario) with no diffraction operator. The top two plots illustrate the attenuation of the pump beam as it travels left to right in the medium and amplification of the probe beam as it travels right to left. Along the y-axis is the time evolution. The pump starts as a transform limited Gaussian profile.

The gain coefficient, Γ is always positive for all points in z and time as shown in Figure 25. For E3PA media, the gain coefficient is defined as

$$\Gamma = \frac{4\pi\sigma_{ref}}{\lambda} |N_{osc}| \sin(\phi - \psi) \tag{71}$$

where $|N_{osc}|$ is equivalent to a modulation depth, ψ is the phase of the interference pattern, and ϕ is the phase of the grating. The term ψ will change over time due to S/XPM effects. The term ϕ is the temporal convolution of ψ and will always lag

insuring that the sine function is negative. This coupled with a negative σ_{ref} creates gain in the probe. An opposite sign in σ_{ref} will place gain in the pump and further attenuate the probe beam. This asymmetry was experimentally verified by [55]. For the Fresnel coupled case, the probe beam is derived from the pump meaning that all accumulated S/XPM in the forward path is transfered to the probe beam. In other words, the probe beam is effectively pre-chirped or conditioned with a time dependent phase. As it travels toward the front of the sample, it sees a pump field with smaller degree of S/XPM with the maximum phase shift between interference pattern and grating occuring near the front of the sample. Consequently, the argument of the sine function in Equation 71 is limited to values less than $\pi/2$ at least for relevant input intensities insuring efficient energy transfer throughout the entire pathlength of the sample.
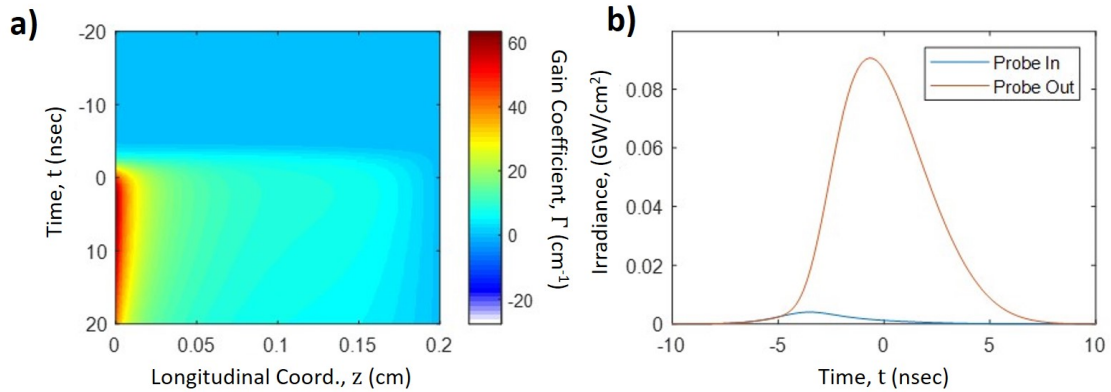
Figure 25. The middle right compares the probe input (the Fresnel reflection of the pump beam on the rear surface) to the probe output. Temporal pulse shaping is apparent. Temporal and longitudinal dependence of the gain coefficient is shown middle left. The value is always positive indicating that energy is always flowing from pump to probe throughout the simulation. A maximum value of 60 cm^{-1} rivals traditional photorefractive media however that value drops dramatically in the sample.

Also evident in 25 is the pulse shaping nature of the interaction. The pump field began as a transform-limited Gaussian beam. The probe output is clearly not Gaussian and indicates that some degree of spectral modulation must be occurring

which is addressed in the next subsection.

Finally, the monotonic decay and growth of the pump and probe respectively is shown in 26 with the maximum output of the probe achieving 16% at the front surface of the sample consistent with experimental results at 532 nm. This monotonic function is a direct result of the positive gain coefficient throughout the space and time. As will be shown in subsequent sections, this behavior is not always typical for other geometries but unique to Fresnel Coupling and speaks to its superior efficiency and ease of observation.
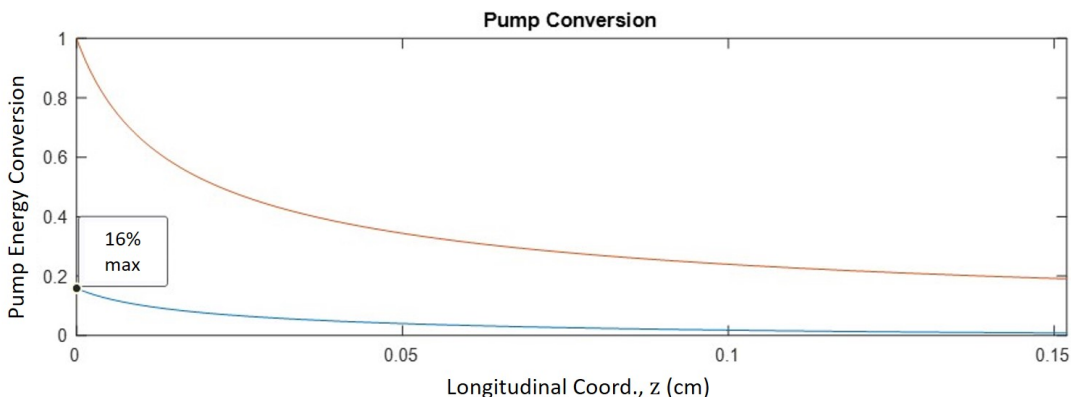
Figure 26. A 16% pump energy transfer is predicted from the numerical model and consistent with experimental results for a solution of 50 mM E1BTF. This result is significantly smaller than the previous results for the same material at 785 nm due to less favorable constitutive parameters at this wavelength.

Spectral Measurements of Fresnel Coupling.

As was mentioned in the previous subsection, when the pump field passes through the sample, temporal pulse shaping occurs as a result of the both amplitude and phase modulation. The probe field is derived from the pump and passes back through the nonlinear wake left by the pump where further pulse shaping occurs from the complex nonlinearity and coupling physics. When the probe exits the sample, the temporal shape may be very different than the initial pump pulse. Furthermore, S/XPM will

61

also add bandwidth through the time dependent phase shifts. Spatially, the intensity distribution of the laser focus will insure this amplitude and phase modulation is not uniform. As a result, the angular frequency spectrum of the probe beam will change and will not be spatially uniform. This can be modeled numerically by transforming the temporal function of the transmitted probe into frequency space and integrating along the radial dimension provides an integrated power spectrum. Figure 27 shows the power spectrum of the transmitted probe field for 1.8 J/cm^2 (Fresnel Derived Probe from Figure 22) compared to experimental data measured using the apparatus described in Figure 18.
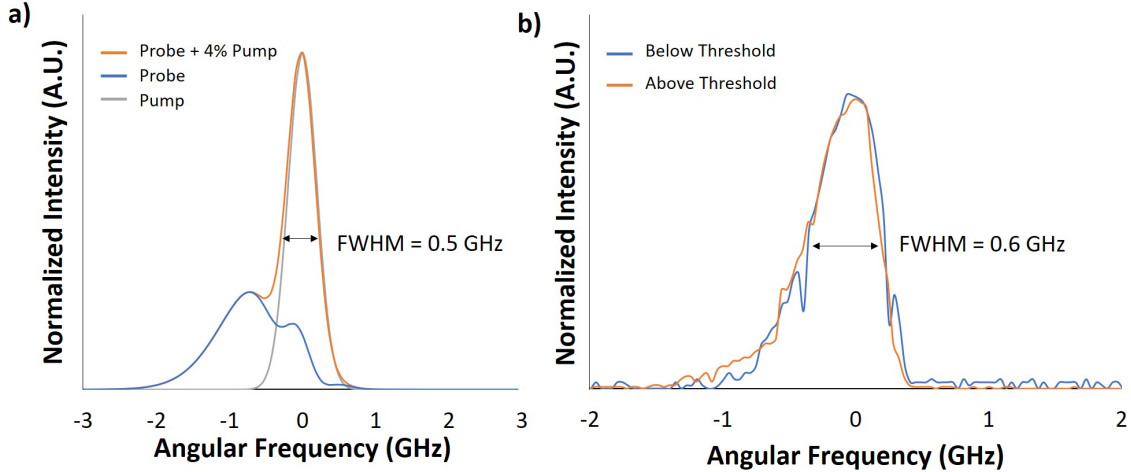
Figure 27. Simulated spectral content of Fresnel coupled beam calculated with a pump beam of 1.8 J/cm^2 compared to experimental results utilizing the Fabry-Perot Etalon apparatus in Figure 18. Experimental FWHM measurements are in strong agreement below and above threshold. Numerical results indicate the Fresnel coupled probe beam should experience a significant increase in bandwidth as well as an approximate 1GHz shift to lower frequency. Experimental confirmation is inconclusive and may be a result of relative power contributions from the pump and probe in the far field measurement.

Through numerical simulations, the Fresnel coupled probe beam sees a significant increase in bandwidth compared to the 0.5 GHz FWHM of the incident pump beam. The amplitude of the pump has been normalized to demonstrate the relative power for a 4% reflection. The experimental measurement would also include this signal from

the front surface reflection indicated by the power sum (orange line of the left hand side). Numerical results would seem to predict a weak but clearly recognizable hump on one side of the residual pump signal. Comparison to the experimental results on the right hand side is inconclusive with perhaps a very small bump on the negative frequency side of the peak above the TBC threshold. However, experimental artifacts cannot be fully discarded. Note that the numerical results fully integrate the spatial extent of the probe in the near field of the sample whereas the experimental results are a smaller spatial sample taken in the far field which may act to reduce the probe spectral contribution to the signal. Regardless, the existence of any signal outside the original pump spectrum was absent. This strongly excludes stimulated Brillouin scattering as a possible explanation and further validates the SRBS/Fresnel Coupled TBC theory of nearly degenerate interaction. Also note that the resolution of the Fabry Perot Etalon used in this work is approximately a 3x improvement from He et. al. measurements [22].

4.2   Two Counter-Propagating Beams

Similar to the Fresnel coupling case, deliberately mixing two degenerate frequency beams also results in one-way energy transfer. As previously discussed, the mechanism for this phenomenon can be explained by inherent chirp in the fields or through the nonlinearities arising from self-action in the media, i.e. S/XPM. The case for chirp is much more relevant for psec pulse where the time-bandwidth product is more favorable. In the nsec pulse regime of interest in this work, the single longitudinal mode laser is effectively transform limited. Apart from this indirect, albeit reasonable, argument for the S/XPM mechanism, the counter-propagating experiment offers direct proof consistent with the work of Dutton et. al. [15].

Consider two beams derived from the same source and routed according to the
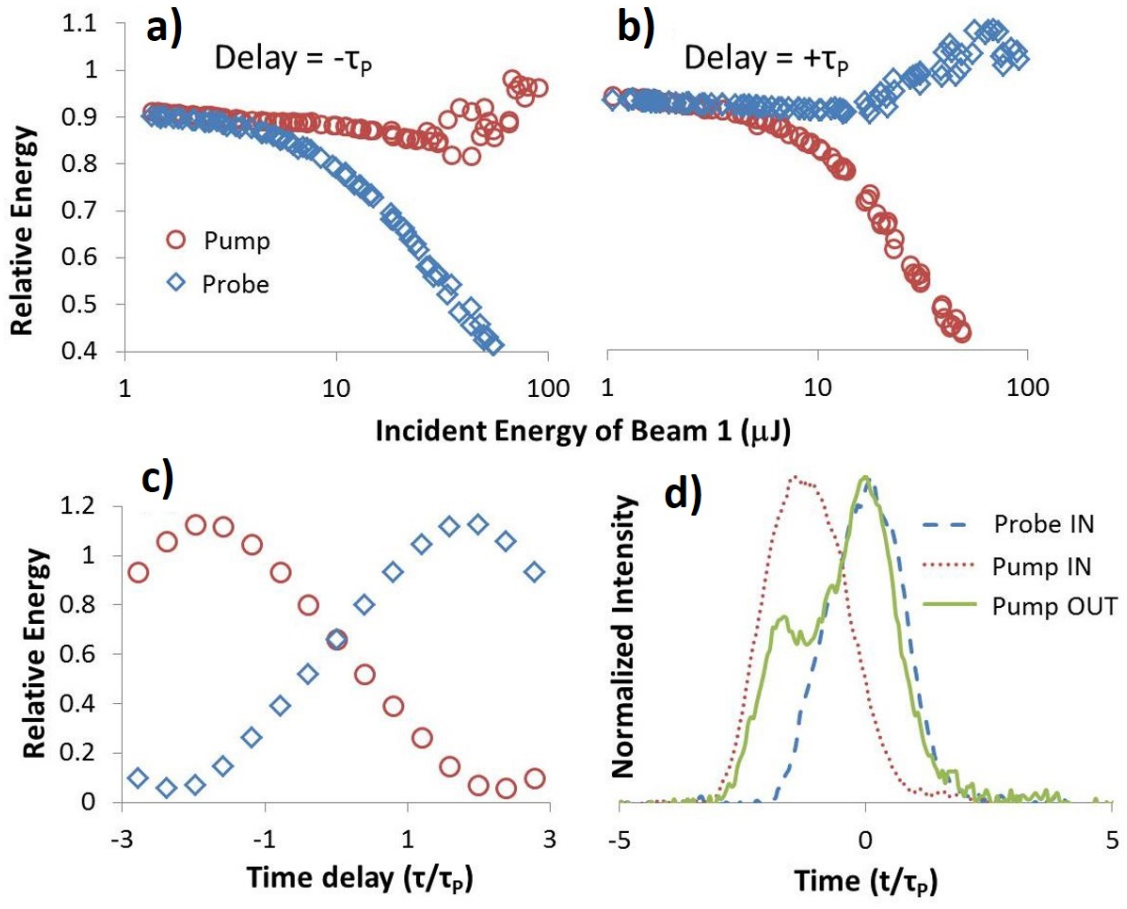
Figure 28. One way energy transfer for 50mM E1BTF solution at 700nm was previously presented for counter-propagating geometry [49]. Experimental results for equal energy beams are shown in (a) and (b) at opposite relative time shifts with respect to zero. The direction of energy transfer is reverse and predicted by the plane wave model (c). Experimental pulse profiles (d) were collected demonstrating energy transfer occurs from the proceeding pulse to the lagging pulse consistent with a negative refractive nonlinearity.
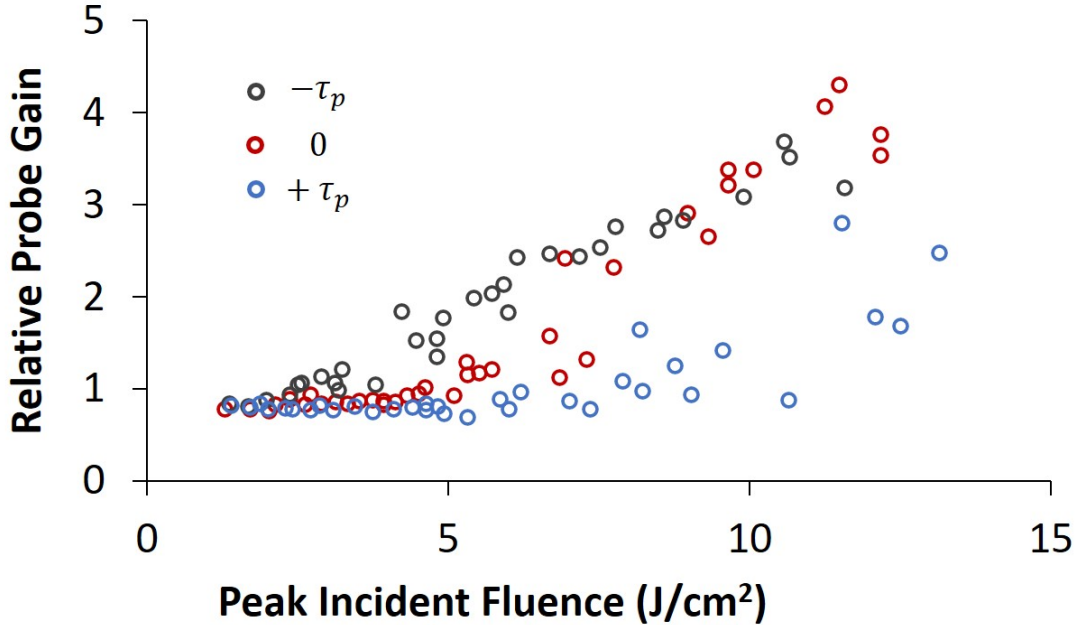
Figure 29. Counter-propagating TBC with attenuated probe beam from Ref [49]. The qualitative reduction in efficiency is apparent. Furthermore, the probe gain at zero time delay is appreciable indicating a S/XPM driven phenomenon.

experimental setup shown in Figure 14. If the beams have equal energy and are focused with the same lens power, the peak irradiance will be identical. Additionally, if the optics are positioned confocal with the focal plane centered in the nonlinear medium, the relative paths through the medium will be identical and the accumulation of S/XPM will also be identical so long as the beams are exactly synced in time such that the peak of the pulses arrive at the focal plane at the same time. As result, the exchange of energy will be symmetric and the net effect will be appear to have no coupling. As one beam is delayed relative to the second, the accumulation of phase modulation becomes asymmetric since the proceeding beam has effectively traveled through more of the sample before temporal overlap starts. In this case, one field is favored and energy transfer may be resolved experimentally. Figure 28 illustrates this nature experimentally. A 50 mM solution of E1BTF was exposed with equal energy pump and probe beams in opposite directions at different relative time

65

shifts. The direction of energy transfer swapped with respect to the zero time delay as expected from the numerical model. Additionally, experimental pulse profiles measured on a 6GHz oscilloscope identified that energy was transfered from proceeding to lagging pulse consistent with a negative refractive nonlinearity. Conversely, a positive nonlinearity would have the opposite effect.
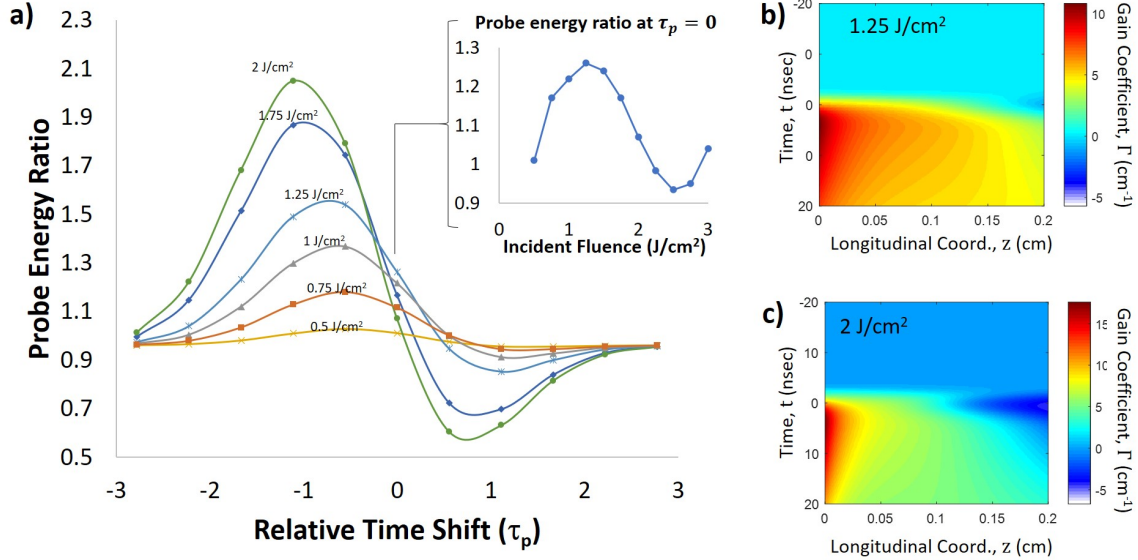
Figure 30. Probe energy ratios for various values of incident fluence and time shift. (Inset top right) The values along zero time delay versus incident fluence have a curious oscillating pattern due to the phase wrapping in the gain coefficient where the holographic grating and interference pattern have shifted greater than 90 degrees. The change in sign is the gain coefficient reduces the overall efficiency of counter-propagating TBC relative to the Fresnel coupled case.

For equal energy beams, the zero-energy transfer location is always at zero relative delay for S/XPM or chirp driven TBC. However, these two mechanisms can be distinguished by introducing asymmetry in the relative energy, i.e. attenuation of one the beams which will be designated the probe. Because the S/XPM mechanism is sensitive to both path length and intensity of the beams, a weaker field will experience less phase modulation even for a zero relative time delay. The chirp driven phenomenon is governed solely on asymmetric temporal overlap in the medium and

is insensitive to intensity [13] thus maintaining the zero-energy transfer at the zero relative time delay regardless of intensity. Figure 29 shows counter-propagating TBC for 50mM E1-BTF at 700nm with an attenuated probe at different relative time delays. Qualitative reduction in efficiency and appreciable probe gain at the zero time delay are indicative of a S/XPM driving mechanism as would be expected for a nsec timescale.

Figure 30 shows the probe energy ratio, i.e. probe out divided by probe in, for various incident peak fluence values and time shifts. The probe energy was kept constant and the pump was increased according the fluence markers. The probe will experience gain for the negative time shift as has already been addressed due to the negative refractive nonlinearity but a curious effect occurs at the zero time delay. Inset in Figure 30 is the probe energy ratio at zero delay versus incident fluence and the trend appears to oscillate. Initially, the gain is modest then grows to peak just above 1 J/cm^2 and then strangely reverses course counter to previous numerical studies [15]. This decay continues until a minimum occurs where energy is actually flowing back into the pump. This course reverses yet again and probe gain grows back in. The reason for this is that the gain coefficient changes sign in the (z,t) plane due to the sine function in Equation 71 and illustrated in Figure 6. If the phase shift between holographic grating and interference drifts beyond 90 degrees, the energy transfer with switch directions and appears to be the case in the simulation. Additionally, the overall efficiency for counter-prop TBC with a weak probe is noticeably weaker than the Fresnel coupled case as evidenced by the weaker gain coefficients. This is presumed to be a result of this phase wrapping and reversal of the gain which is absent in the Fresnel case due to the fact that probe field is always derived from the pump field and is therefore pre-conditioned, or pre-chirped, due to the double pass nature of that phenomenon.

Coherent Amplification.
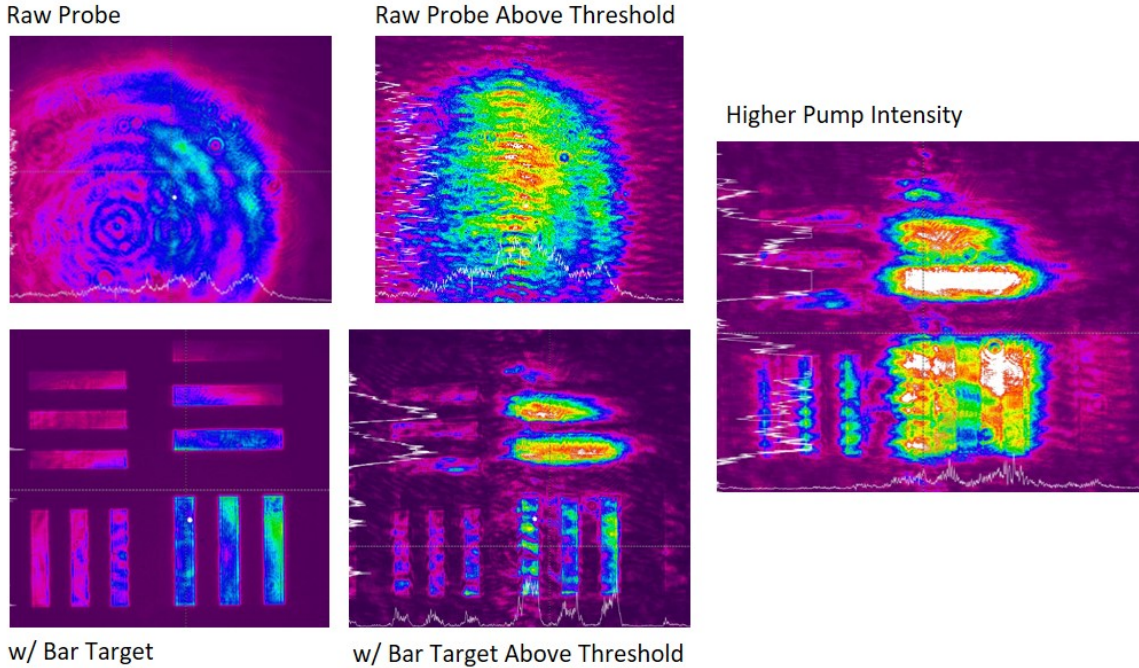
Figure 31. Experimental verification of coherent amplification using a bar target arranged in a 4*f* optical geometry. Just above threshold, probe gain is apparent with and without the bar target object in place. A higher pump intensities, the spatial information begins to distort likely from intrinsic blooming from the negative nonlinear index of refraction. However, the bar target is still clearly discernible.

Recently, we were able to show in the laboratory that energy transfer in degenerate frequency TBC is indeed coherent by placing the coupling medium at the Fourier plane of a bar target object illuminated by a weak beam (see Figure 15). We then aligned a strong pump field to overlap the weak beam in the Fourier plane and were able to observe a qualitative increase in the bar target image intensity. Without the bar target in place, amplification is also present in the raw probe where the energy in the beam profile is strongest in the lop left-hand side. This is of course a result of the nonlinear mechanism is also present when the transparency is in place. For example, in the lower left figures, the energy is not uniformly illuminated on the bars and the area of highest intensity sees the amplification.

The coherent amplification had a frequency of greater than 10Hz which was the upper limit of the imaging camera and the rep rate of the pump laser. It is likely this can be much larger since we know the nonlinear lifetime is on the order of 100s of nanoseconds enabling cycle times of kHz to MHz. There is a loss of contrast which is to be expected given the nonlinearity which preferentially couples on axis providing a effective low pass filter. Additionally, the negative nonlinear refraction results in a strong blooming effect. Still the features of the bar target are clearly discernible. It should also be noted that this is clearly not phase conjugate interaction as has been described by He et. al. [22]. Indeed, the presence of far field blooming the Fresnel coupled beam are clear indications that the process is not a phase conjugate interaction, and futhermore, TBC by definition is not a phase conjugation mixing process.

This coherent amplification can also be demonstrated with the numerical radial beam propagation recipe. However, in order to propagate the beams between the near and far fields relative to the sample, a linear transfer function must be included. Figure 32 illustrates the simulation. First, the weak probe beam is defined as a contrast object of concentric rings analogous to the rectilinear bar target example shown experimentally. This amplitude function with uniform phase is propagated to the lens using the Fresnel integral such that

$$E_2(r_2, z) = \frac{ke^{ikz}}{iz} e^{\frac{ikr_2^2}{2z}} \int_0^\infty r_1 E_1(r_1) e^{\frac{ikr_1^2}{2z}} J_0\left(\frac{k}{z} r_1 r_2\right) dr_1. \tag{72}$$

The integral is solved numerically in MATLAB. Once at the lens location, the lens function is applied such that

$$E_2(r_2) = E_1(r_1) e^{\frac{-ikr_1^2}{2f}} \tag{73}$$
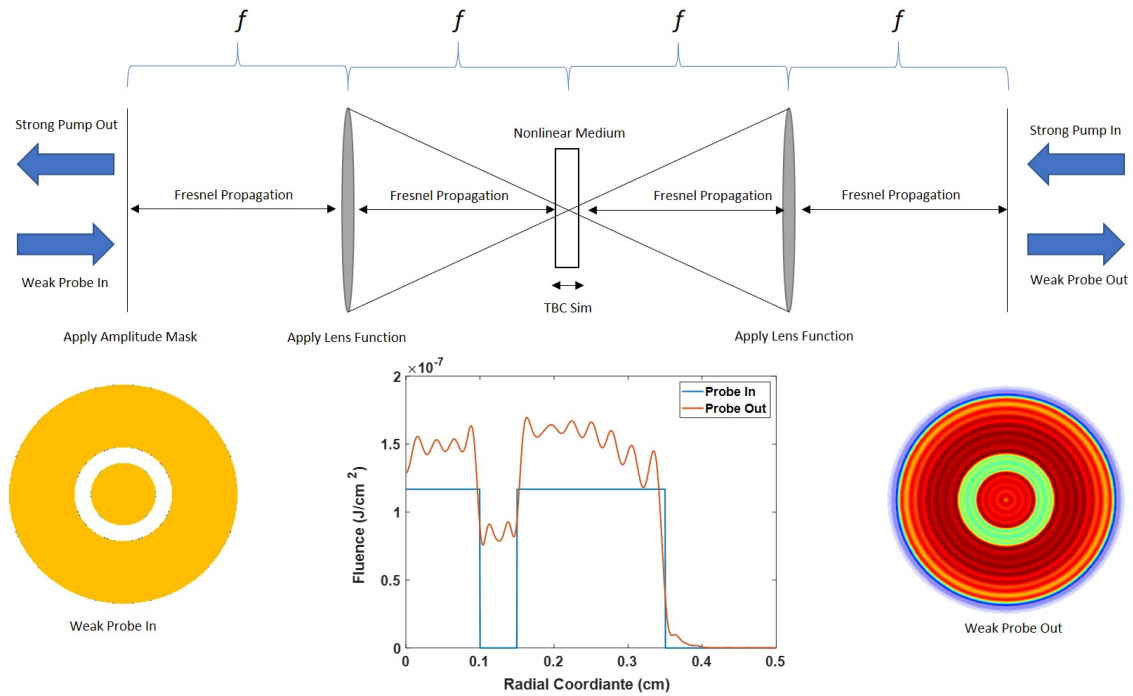
Figure 32. Coherent amplification simulation illustrating the transfer of spatial phase information from a weak probe beam consisting of concentric rings. The probe is propagated from input to lens to sample using a numerical evaluation of the Fresnel integral which allows for resampling the near the focal plane. The pump field is analytically evaluated at the opposite side fo the sample and the numerical counter-propagation TBC recipe is used to calculate the exit probe field. A series of Fresnel transfer functions and lens function is completed to render the amplified probe field in the observation plane. Gain and spatial blooming are evident in the radial cross-sections consistent with experiment.

where f is the focal length of the lens. Next, the probe field is propagated with the Fresnel integral to the entrance plane of the sample which allows for rescaling of the radial coordinate which is not available in the Hankel propagator. This resampling provides a greater resolution at the much smaller spatial scale of the focal plane and additionally allows for sampling with the specific Bessel zeros algorithm required for the Hankel propagator. The pump field is analytically calculated at the opposite end of the sample and the TBC numerical simulation is applied. The resultant probe field is then propagated out to the second lens again using the Fresnel integral. The second lens function is applied followed by free space propagation the observation plane. The input and amplified probe spatial distributions are rendered in Figure 32. Amplification as well a blooming is present in the radial cross section consistent with the experimental results.

Contrast or modulation loss is a direct result of the intensity dependent nonlinearities and the spatial distribution of the pump and probe in the Fourier plane. Due to this effect, the gain profile takes a spatial distribution that favors energy on axis and effectively acts as a low pass filter. Additionally, the same phenomenon generates a weak lensing effect that blooms the output in the image plane. This is unfortunately a practical limitation of the experimental setup. Due to the high fluence necessary to drive coupling, approximately 1 J/cm^2, the sample had to be placed in the laser focus. Theoretically, if a plane wave input can be achieve with the requisite intensity, e.g. in the near field of a pulsed laser, it may be possible to eliminate these deleterious spatial blooming and low pass filtering effects. This may be useful for power scaling and holographic amplification applications. Additionally, even the Fourier plane, the low frequency information of the target is apparent and may still be useful for applications involving compressive sensing where object detail is less important, e.g. autonomous vehicles.

This concept can be easily applied to arbitrary rectilinear fields by implementing a fast, Fourier transform (FFT) formalism. However, this comes with the obvious computation cost due to the larger memory requirements.

4.3   Two Co-Propagation Beams

The most glaring result of this work was the apparent absence of degenerate frequency TBC in the co-propagating geometry for any semiconductor or organic dye system. Given the experimental results of previous works presented in Chapter 1 [13, 15, 55] and the steady-state models for Kerr media [46, 8], this absence was surprising. A great deal of care was put into adjusting multiple relative temporal delays. Both positive and negative delays of the probe were considered relative to the pump, i.e. cases where either the probe proceeded or lagged. Various relative probe intensities were also considered from a ratio of 1:1 to 1:0.001. Ultimately, the CFP was employed to insure optimal spatial overlap in the nonlinear media. However, for each permutation, co-propagating TBC was simply absent.

Figure 33. Co-propagating TBC with 50mM E1BTF in solution with a weak probe beam and shallow angle of incidence. The rapid cycling of the gain coefficient leads to negligible energy transfer over the 2mm path length of the cuvette. Numerical simulations would indicate that a much thinner sample may have a significantly higher coupling efficiency as the "coherence length" compresses to shorter and shorter path lengths and larger gain coefficients.

The reason for this can be explained in Figure 33 which shows the simulated gain profile for a co-propagation geometry. Recall the effect of the sine function with respect to the gain coefficient in the counter propagating scenario. This effect is even larger in the co-propagting geometry and expresses itself in the form of self-oscillation and causes energy transfer to swap directions rapidly as shown in 34. This effect is present regardless of relative time shift and is unique to the co-propagating geometry as the probe field only experiences gain in the wake of the strong pump field and consequently observes intense cross-phase modulation.

Figure 34. Co-propagating TBC with 50mM E1BTF in solution with a weak probe beam and shallow angle of incidence. The rapid cycling of the gain coefficient leads to negligible energy transfer over the 2mm path length of the cuvette. Numerical simulations would indicate that a much thinner sample may have a significantly higher coupling efficiency as the "coherence length" compresses to shorter and shorter path lengths and larger gain coefficients.

In Figure 35, we can see that for our 2 mm sample, the coupling with a weak probe beam would appear to be minimal. This has the qualitative effect of a coherence length although physically different than the quasi-phase matching. That is, if the sample was 200 microns thick, co-propagation coupling may have been observed. This of course will require more experimental work to validate but the prediction for self-oscillation in this geometry would seem to indicate TBC in co-propagating fields

for S/XPM-driven TBC is challenging but not impossible. Furthermore, the amplitude of the gain coefficients are significantly larger than even the Fresnel coupling case indicating that under the right circumstances, co-propagation may be extremely efficient. At the 200 micron optimum thickness the energy transfer exceeds 70%.
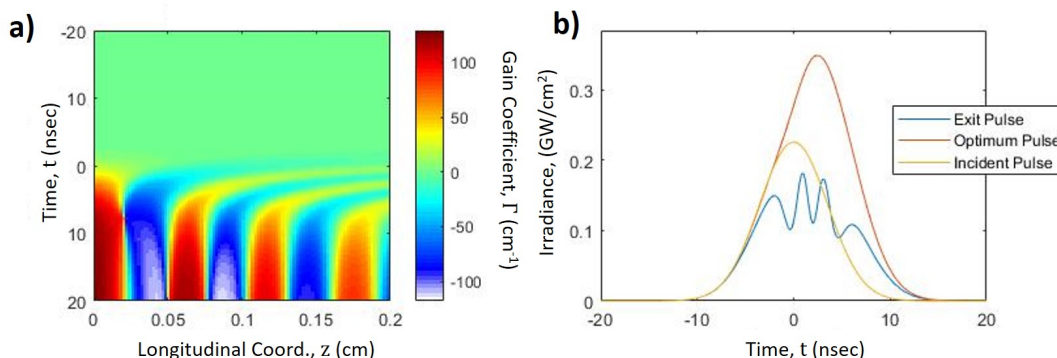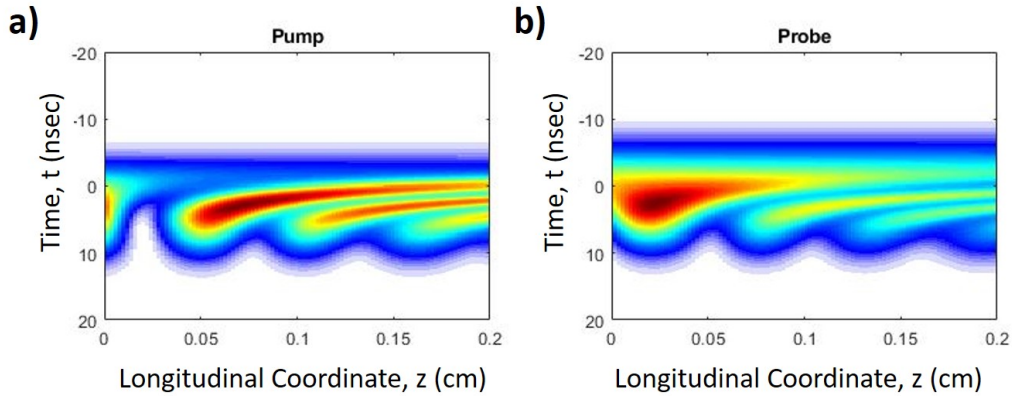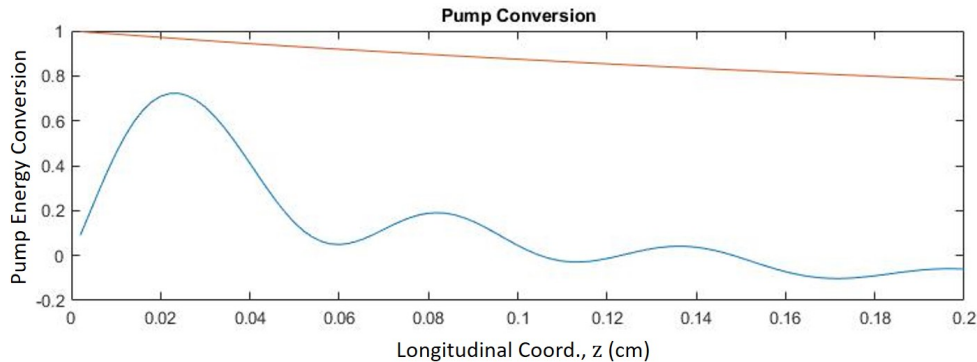

Figure 35. Co-propagating TBC with 50mM E1BTF in solution with a weak probe beam and shallow angle of incidence. The rapid cycling of the gain coefficient leads to negligible energy transfer over the 2mm path length of the cuvette. Numerical simulations would indicate that a much thinner sample may have a significantly higher coupling efficiency as the "coherence length" compresses to shorter and shorter path lengths and larger gain coefficients.

4.4 Degenerate TBC in Semiconductor Media

Our most recent work employed E3PA organic dye molecules in solution. While this may be acceptable for some applications, a solid state solution is desirable for practical purposes. In general, there is no reason that this phenomenon should not occur 2PA/FCR active semiconductor media. In fact, the nonlinearities may be significantly larger [9] and because this type of media can be pumped in the band gap, there is negligible linear losses. The challenge with these materials lies in the free carrier lifetime. Since the resonant nonlinearity is a result of the free carrier refraction, it is critical these carriers live long enough to facilitate energy transfer. Therefore we may need to characterize the lifetimes of the nonlinearities via pump/probe spec-
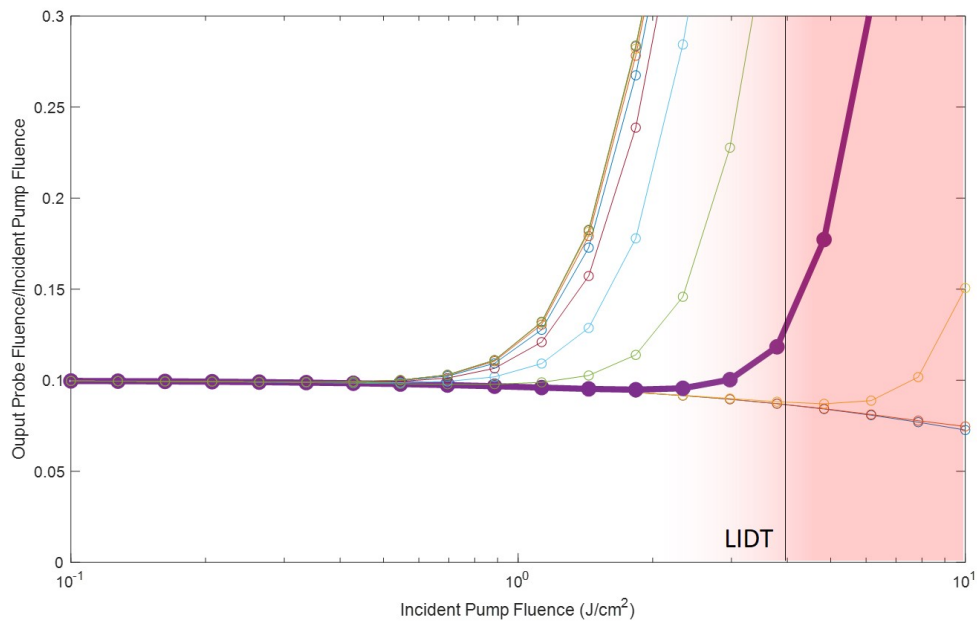
Figure 36. Energy transfer for co-propagating fields in semiconductor media with increasing free carrier lifetime. Single shot LIDT occurs at approximately 4 J/cm². The bold, purple line indicates the expected 10nsec lifetime of high quality ZnSe but the gain occurs near the LIDT horizon making TBC observation challenging.

troscopy. A high quality ZnSe sample was tested at 532nm in each geometry and TBC was not observed for any permutation. Furthermore, low laser induced damage was observed near the nonlinear threshold which limited pump intensity to levels that are expected to be below the TBC signal gain for ZnSe carrier lifetimes. TBC simulations for ZnSe are shown in 36. Each curves shows the quadratic gain in TBC signal with increasing nonlinear lifetime. The bold line indicates the expected result for ZnSe with the shaded red region signifying the observation of laser induced damage.

V. Conclusions

Degenerate frequency TBC has a rich history in nonlinear Kerr media dating back forty years examining chirp and phase-modulation driven mechanisms. Previous studies focused almost exclusively in psec excitation for the high peak intensities and large spectral bandwidths those sources. Due to the relatively weak nonlinearities present at that timescale, the observations were largely treated as deleterious effects in ultrafast spectroscopy or laser cavity efficiencies and practical uses in holographic amplification for degenerate frequency TBC were never fully realized. The phenomenon may have been relegated to obscure corners of nonlinear optics if not for the emergence SRBS in resonant Kerr media in the mid-2000s. The strong coupling efficiencies achieved in SRBS would seem to overcome a practical limitation in temporal responsivity present in traditional photorefractive devices, or reciprocity failure. The academic communities working SRBS have responded with material science engineering of the resonant Kerr media in an attempt to optimize the coupling signal. However, without a comprehensive analytical model, progress has been limited. This work provides such a model both in theory and numerical analysis to inform ongoing material development.

From the experimental and computational results in this work, it is apparent that the accumulation of S/XPM is strongly dependent upon the directionality and asymmetry of the pump and probe fields. For example, energy exchange between co-propagating beams in E3PA and semiconductor media is virtually non-existent experimentally regardless of asymmetry because of the presence of self-oscillation or phase wrapping in the gain coefficient. Counter-propagating fields do exhibit modest energy exchange and have been shown in this work to amplify phase information in the form of a bar target transparency image. Finally, the most efficient case occurs when the probe field is derived from the pump through some means of elastic scattering

with the most efficient in terms of threshold being the Fresnel reflection from the rear surface of the sample. It has been shown in this work that in this case, phase wrapping and self oscillation is suppressed for relevant pump intensities due to the effective pre-conditioning of probe signal due to the unique geometry.

This Fresnel case is the source of much interest in the SUNY-Buffalo group of He et. al. studying SRBS. With the model and numerical simulation provided in this work, we have identified the important material parameters and resolved the geometrical constraints that govern degenerate frequency S/XPM-driven TBC. With this understanding, it is now possible to begin the next process of application. The material engineering by the SUNY-Buffalo group evidenced by the SRBS to SMS transition may be greatly informed by this analytical and numerical model. Furthermore, the compounding evidence for the presented theory indicate the direct connection from the antecedent work of Dutton et. al. to He et. al. and reconciles degenerate frequency TBC of all forms with established nonlinear optics and dynamic holography.

As outlined in the introduction, one of our goals is to show experimentally that for degenerate frequency TBC is a viable option for real time holographic applications. We have qualitatively shown this by amplifying the bar target image at a refresh rate of at 10Hz. This is dramatic improvement in terms of cycle time relative to transitional photorefractive media [2] and overcomes the reciprocity failure of those devices. While the gratings for S/XPM-driven TBC have been quantified and shown to be on the order of photorefractive devices, the overall efficiencies are still quite weak. The next stage of this work will require a deeper investigation using the numerical tools provided here to engineer materials and optical geometries that can be optimized for power scaling and coherent transfer. For example, we know that in Fresnel coupling the probe field is derived from the pump field with a preconditioned temporal phase and that this is the reason the gain coefficient is alway positive. It

may be possible to utilize this same concept by pre-conditioning pump or probe fields externally before the coupling stage to optimize efficiency. In fact this is addressed in a US Patent filed and awarded in this effort [51].

The numerical recipe presented in the work is comprehensive informing power scaling and coherent amplification application space. Furthermore, the coherent amplification experimental results conclude that the phase transfer effect are not phase conjugate but rather phase additions which may also enable analog compressive sensing technology by extending this work to rectilinear FFT linear operators. For example, by mixing the object signal with an orthogonal basis set of spatial phase functions, one may be able to reconstruct the object with just a limited number of pulses.

Solid state media such a semiconductors and specifically small band gap semiconductors may ultimately be the ideal media. However, this will require reliable experimental work in the short-wave or mid-wave infrared. Large band-gap media such as ZnSe contained neither the requisite lifetime nor sufficient LIDT to produce measurable, reliable TBC of any kind in this work.

Spectral bandwidth measurements and calculations were also presented in the work and consistent with previous works of He et. al. The nonlinear Fresnel coupled signal and presumably the SRBS signal are clearly degenerate frequency interactions void of any influence of Brillouin scattering. The nomenclature of degenerate frequency is subject to interpretation as calculations indicate that some degree of phase modulation is required for coupling to occur which must result in a frequency shift or increase in bandwidth. The magnitude of this frequency manipulation however may simply be too small to resolve even with Fabry Perot Etalon evaluation.

The next chapter of degenerate frequency TBC may be informed by this work and certainly the theoretical predictions will require experimental validation. Future work

79

must test and confirm the apparent path length dependence in the co-propagating geometry and the concept of pre-conditioning the pump and/or probe fields for signal optimization must be reduced to practice. Once these predictions can be experimentally controlled, practical engineering for pulsed laser power scaling and holographic amplification can be addressed. For example, with proper path lengths and pre-conditioning, the optimal pulse overlap for high efficiency energy transfer may be achieved.

VI. Appendix

Table 1 collates nonlinear optical parameters for representative E3PA organic media. E1BTF and Silicon Naphthalocyanine (SiNc) have been well characterized by the community and references are provided. Benzophenone is a unique case as this material is capable of melt processing into a super-cooled glass at neat concentrations. Fresnel coupling in neat Benzophenone is easily observed at 532 nm. However, due to the relatively weak nonlinearities in this system, deliberate counter-propagation coupling is negligible. Fresnel coupling in SiNc solutions are also observable but due to strong ground state absorption and solubility limits, counter-propagation coupling was not observed.

Table 1. Linear and nonlinear optical parameters for organic media.

Parameter	E1BTF (THF)	E1BTF (THF)	Benzophenone (Neat)	SiNc (Toluene)
λ (nm)	785	532	532	532
n	1.4073 [12]	1.4073 [12]	1.638[a]	1.5019 [29]
Conc. (M)	0.05	0.05	6.09[b]	0.005
ϵ_0 (M^{-1} cm^{-1})	0.2	4.0	4.7x10^{-3}	740 [59]
σ_0 (/10^{-21} cm^{-2})	0.76	15.4	1.8x10^{-3}	2830
β (cm/GW)	1.0	1.0	3.0	0
σ_2 (GM)	840 [40]	0	30.6[a]	0
γ (/10^{-5}cm^2/GW)	5.3[c]	5.3[c]	1.8x10[a]	5.3x10^{59}
ϵ_T (M^{-1} cm^{-1})	47000[40]	38000[40]	7200 [10]	40000 [59]
ϵ_S (M^{-1} cm^{-1})	0	0	0	10200 [59]
ϕ_T	1[40]	1[40]	1 [10]	0.2 [59]
σ_{abs} (/10^{-17}cm^2)	17.9	3.0	2.75	15.3[d]
σ_{ref} (/10^{-21}cm^3)	-1	-1	-1	-1

[a] This work.

[b] Estimated from mol. wt. and density.

[c] Estimated from toluene data.

[d] Effective cross section using formalism of [54].

Bibliography

[1] P.-A. Blanche, B. Lynn, R. A. Norwood, and N. Peyghambarian. Advances in photorefractive polymers and applications. *Proceedings: SPIE*, 9564, Sep 2015.

[2] P.-A. Blanche, B. Lynn, D. Churin, K. Kieu, R. A. Norwood, and N. Peyghambarian. Diffraction response of photorefractive polymers over nine orders of magnitude of pulse duration. *Sci. Rep.*, 6:29027, 2016.

[3] R. Bonifacio, M. Gronchi, and L. A. Lugiato. Self-pulsing in bistable absorption. *Opt. Commun.*, 30:129–133, 1979.

[4] M. Born and E. Wolf. *Principles of Optics*. Pergamon, 1980.

[5] G. Boudebs, M. Chis, and J. Bourdin. Third-order susceptibility measurements by nonlinear image processing. *J. Opt. Soc. Am. B*, 13:1450–56, 1996.

[6] R. W. Boyd. *Nonlinear Optics*. Academic Press, 2013.

[7] B. Butcher and D. Cotter. *The Elements of Nonlinear Optics*. Cambridge University Press, 1990.

[8] M. Chi, J.-P. Huignard, and P. M. Petersen. A general theory of two-wave mixing in nonlinear media. *J. Opt. Soc. Am. B*, 26(8):1578, 2009.

[9] D. N. Christodoulides, I. C. Khoo, G. J. Salamo, G. I. Stegeman, and E. W. V. Stryland. Nonlinear refraction and absorption: mechanisms and magnitudes. *Adv. Opt. Photon.*, 2(1):60–200, 2010.

[10] R. H. Compton, K. T. V. Grattan, and T. Morrow. Extinction coefficients and quantum yields for triplet-triplet absorption using laser flash photolysis. *J. Photochem.*, 14:61–66, 1980.

[11] A. Couairon, E. Brambilla, T. Corti, D. Majus, O. de J. Ramírez-Góngora, and M. Kolesik. Practitioner's guide to laser pulse propagation models and simulation. *Eur. Phys. J.*, 199(1):5–76, 2011.

[12] F. E. Critchfield, J. A. Gibson, and J. L. Hall. Dielectric constant and refractive index from 20 to 35 degrees and density at 25 degrees for the system tetrahydrofuran-water. *ACS Pub.*, 75:6044–6045, 1953.

[13] A. Dogariu, T. Xia, D. J. Hagan, A. A. Said, E. W. V. Stryland, and N. Bloembergen. Purely refractive transient energy transfer by stimulated rayleigh-wing scattering. *J. Opt. Soc. Am. B*, 14(4):796–803, 1997.

[14] M. Drobizhev, N. S. Makarov, T. Hughes, and A. Rebane. Resonance enhancement of two-photon absorption in fluorescent proteins. *J. Chem. Phys. B*, 111: 14051–14054, 2007.

[15] T. E. Dutton, P. M. Rentzepis, T. P. Shen, J. Scholl, and D. Rogovin. Picosecond degenerate two-wave mixing. *J. Opt. Soc. Am. B*, 9(10):1843–1849, 1992.

[16] W. J. Firth. Stability of nonlinear fabry-perot resonators. *Opt. Commun.*, 39: 343–346, 1981.

[17] H. M. Gibbs, F. A. Hopf, D. L. Kaplan, and R. L. Shoemaker. Observation of chaos in optical bistability. *Phys. Rev. Lett.*, 46:474–477, 1981.

[18] L. P. Gonzalez. Accurate determination of nonlinear optical parameters of semiconductors at infrared wavelengths. *University of Dayton*, Ph. D. Thesis, 2009.

[19] L. P. Gonzalez, J. M. Murray, V. M. Cowan, and S. Guha. Measurement of nonlinear optical properties of semiconductors using the irradiance scan technique. *Proceedings: SPIE*, 68750R1-5, 2008.

[20] M. Guizar-Sicairos and J. C. Gutiérrez-Vega. Computation of quasi-discrete hankel transforms of integer order for propagating optical wave fields. *J. Opt. Soc. Am. A*, 21:53–58, 2004.

[21] P. Gunter and J. Huignard. *Photorefractive Materials and Their Applications*. Springer-Verlag, 2007.

[22] G. S. He. *Progress in Optics Chapter 4: Stimulated Scattering Effects of Intense Coherent Light*, volume 53. Elsevier, 2009.

[23] G. S. He, T.-C. Lin, and P. N. Prasad. Stimulated rayleigh-bragg scattering enhanced by two-photon excitation. *Opt. Express*, 12:5952, 2004.

[24] G. S. He, L. Changgui, Z. Qingdong, P. N. Prasad, P. Zerom, R. W. Boyd, and M. Samoc. Stimulated rayleigh-bragg scattering in two-photon absorbing media. *Phys. Rev. A*, 71(6):063810–063810.10, 2005.

[25] G. S. He, k.-T. Yong, H.-Y. Qin, Q. Zheng, P. N. Prasad, S. He, and H. Agren. Stimulated rayleigh–bragg scattering from a two-photon absorbing cdse cds zns quantum-rods system: Optical power limiting and phase-conjugation. *IEEE J. Quantum Electron.*, 44:894–901, 2008.

[26] G. S. He, M. Liu, J. W. Haus, M. T. Swihart, and P. N. Prasad. Strong stimulated mie scattering from plasmonic cus nanocrystals in toluene or pentane. *IEEE J. Sel. Top. Quantum Electron.*, 23:1–6, 2017.

[27] G. S. He, W. Hu, A. Baev, R. Kannan, L.-S. Tan, and P. N. Prasad. Mechanism of stimulated mie scattering: Light-induced redistribution of self-assembled nanospheres of two-photon absorbing chromophore. *J. Chem. Phys.*, 151:104202, 2019.

[28] K. Ikeda, H. Daido, and O. Akimoto. Optical turbulence: Chaotic behavior of transmitted light from a ring cavity. *Phys. Rev. Lett.*, 45:709–712, 1980.

[29] S. Kedenburg, T. Vieweg, T. Gissibl, and H. Giessen. Linear refractive index and absorption measurements of nonlinear optical liquids in the visible and near-infrared spectral region. *Opt. Mater. Express*, 2(11):1588–1611, 2012.

[30] H. Kogelnik. Coupled Wave Theory for Thick Hologram Gratings. *Bell Labs Tech. J.*, 48(9):2909–2947, 1969.

[31] S. Krishnamurthy, Z. G. Yu, L. Gonzalez, and S. Guha. Accurate evaluation of nonlinear absorption coefficients in inas, insb, and hgcdte alloys. *J. App. Phys.*, 101:113104, 2007.

[32] N. Kukhtarev, V. Markov, and S. Odulov. Transient energy transfer during hologram formation in linbo3 in external electric field. *Opt. Commun.*, 23:338–343, 1977.

[33] N. V. Kuktarev, V. B. Markov, S. G. Odoulov, M. S. Soskin, and V. L. Vinetskii. Holographic storage in electro optic crystals: beam coupling and light amplification. *Ferroelectrics*, 22:961, 1979.

[34] D. Kvosh, D. Hagan, and E. Van Stryland. Numerical modeling of thermal refraction inliquids in the transient regime. *Opt. Express*, 4(8):315–327, 1999.

[35] D. G. McLean, R. L. Sutherland, J. E. Rogers, J. E. Slagle, M. C. Brant, and P. A. Fleitz. Interpretation of two photon absorption driven nonlinear absorption. *Proceedings: SPIE*, 593401-1, 2005.

[36] K. Novak. *Numerical Methods for Scientific Computing*. Lulu, Aug 2018.

[37] P. Powers and J. Haus. *Fundamentals of Nonlinear Optics*. CRC Press, 2017.

[38] S. Riehemann, G. Von Bally, B. I. Sturman, and S. G. Odoulov. Third-order susceptibility measurements by nonlinear image processing. *App. Phys. B*, 65: 535–539, 1997.

[39] J. E. Rogers, J. E. Slagle, D. G. McLean, R. L. Sutherland, B. Sankaran, R. Kannan, L.-S. Tan, and P. A. Fleitz. Understanding the one-photon photophysical properties of a two-photon absorbing chromophore. *J. Phys. Chem. A*, 108: 5514–5520, 2004.

[40] J. E. Rogers, J. E. Slagle, D. M. Krein, A. R. Burke, B. C. Hall, A. Fratini, D. G. McLean, P. A. Fleitz, C. T. M., M. Drobizhev, S. Markarov, A. Rebane, K. Y. Kim, R. Farley, and K. S. Schanze. Platinum acetylide two-photon chromophores. *Inorg. Chem.*, 46:6483–6494, 2007.

[41] A. A. Said, M. Sheik-Bahae, D. J. Hagan, T. H. Wei, J. Wang, J. Young, and E. W. Van Stryland. Determination of bound-electronic and free-carrier nonlinearities in znse,gaas, cdte, and znte. *J. Opt. Soc. Am. B*, 9:405, 1992.

[42] M. Sheik-Bahae, A. A. Said, T.-H. Wei, D. J. Hagan, and E. W. Van Stryland. Sensitive measurement of optical nonlinearities using a single beam. *IEEE J. Quantum Electron.*, 26:760–769, 1990.

[43] Y. Shen. *The Principles of Nonlinear Optics*. Wiley, 1984.

[44] H. Shu. Split step solution in the iteration of the beam propagation method for analyzing bragg gratings. *Appl. Opt.*, 48:4794, 2009.

[45] Y. Silberberg and I. Bar-Joseph. Instabilities, self-oscillation, and chaos in a simple nonlinear optical interaction. *Phys. Rev. Lett.*, 48:1541–1543, 1982.

[46] Y. Silberberg and I. Bar-Joseph. Optical instabilities in a nonlinear kerr medium. *J. Opt. Soc. Am. B*, 1:662–670, 1984.

[47] J. Slagle, D. Lombardo, S. Trivedi, and S. Guha. Nonlinear optical properties of single crystal cadmium magnesium telluride. *Proceedings: SPIE*, 93591, 2015.

[48] J. E. Slagle. Degenerate frequency two beam coupling in organic media via phase modulation. *University of Dayton*, Master's Thesis, 2014.

[49] J. E. Slagle, J. W. Haus, S. Guha, D. G. McLean, D. M. Krein, and T. M. Cooper. Degenerate frequency two-beam coupling in organic media via phase modulation with nanosecond pulses. *J. Opt. Soc. Am. B*, 33(2):180–188, 2016.

[50] J. E. Slagle, J. W. Haus, D. G. McLean, and S. Guha. Degenerate frequency two beam coupling in organic solutions using nanosecond laser pulses. *Proceedings: SPIE*, 99390, 2016.

[51] J. E. Slagle, S. Guha, and J. E. Haley. Coherent amplification using phase modulated two beam coupling, U.S. Patent 10,079,465, Sept. 2018.

[52] R. L. Sutherland. *Handbook of Nonlinear Optics*. CRC Press, Apr 2003.

[53] R. L. Sutherland. Energy transfer between incident laser and elastically backscattered waves in nonlinear absorption media. *Opt. Express*, 13(24):9788–9795, 2005.

[54] R. L. Sutherland, M. C. Brant, J. Heinrichs, J. E. Rogers, J. E. Slagle, D. G. McLean, and P. A. Fleitz. Excited-state characterization and effective three-photon absorption model of two-photon-induced excited-state absorption in organic push-pull charge-transfer chromophores. *J. Opt. Soc. Am. B*, 22(9):1939–1948, Sep 2005.

[55] M. Sylla and G. Rivoire. Degenerate two-beam coupling polarization properties in nonlinear materials. *J. Opt. Soc. Am.*, 18(11):1612–1619, 2001.

[56] N. Tang and R. L. Sutherland. Time-domain theory for pump–probe experiments with chirped pulses. *J. Opt. Soc. Am. B*, 14(12):3412–3423, 1997.

[57] E. W. Van Stryland, H. Vanherzeele, M. A. Woodall, M. J. Soileau, A. L. Smirl, S. Guha, and T. F. Boggess. Two photon absorption, nonlinear refraction, and optical limiting in semiconductors. *Opt. Eng.*, 24(4):244613, 1985.

[58] A. .von Jena and H. E. Lessing. Coherent coupling effects in picosecond absorption experiments. *Appl. Phys.*, 19:131–144, 1979.

[59] T. H. Wie, D. J. Hagan, M. J. Sence, E. W. Van Stryland, J. W. Perry, and D. R. Coulter. Direct measurements of nonlinear absorption and refraction in solutions of phthalocyanines. *App. Phys. B*, 54:46–51, 1992.

[60] H. G. Winful and G. D. Cooperman. Self-pulsing and chaos in distributed feedback bistable optical devices. *Appl. Phys. Lett.*, 40:298–300, 1982.

[61] P. Yeh. Contra-directional two-wave mixing in photorefractive media. *Opt. Commun.*, 45:323–326, 1983.

[62] P. Yeh. Exact solution of a nonlinear model of two-wave mixing in kerr media. *J. Opt. Soc. Am. B*, 3:747, 1986.

[63] P. Yeh. Two-wave mixing in nonlinear media. *IEEE J. Quantum Electron.*, 25 (3):484–519, 1989.

REPORT DOCUMENTATION PAGE

Form Approved
OMB No. 0704–0188

1. REPORT DATE *(DD–MM–YYYY)*	2. REPORT TYPE	3. DATES COVERED *(From — To)*
01–29–2021	PhD Thesis	Jan 2017 — Jan 2021

4. TITLE AND SUBTITLE

DYNAMIC HOLOGRAPHY IN RESONANT NONLINEAR MEDIA THEORY AND APPLICATION

5a. CONTRACT NUMBER

5b. GRANT NUMBER

5c. PROGRAM ELEMENT NUMBER

6. AUTHOR(S)

Jonathan E. Slagle

5d. PROJECT NUMBER

5e. TASK NUMBER

5f. WORK UNIT NUMBER

7. PERFORMING ORGANIZATION NAME(S) AND ADDRESS(ES)

Air Force Institute of Technology
Graduate School of Engineering and Management (AFIT/EN)
2950 Hobson Way
WPAFB OH 45433-7765

8. PERFORMING ORGANIZATION REPORT NUMBER

AFIT-ENP-DS-21-M-327

9. SPONSORING / MONITORING AGENCY NAME(S) AND ADDRESS(ES)

Department of Engineering Physics
2950 Hobson Way
WPAFB OH 45433-7765
DSN 785-1829, COMM 937-255-1829
Email: jonathan.slagle.2@us.af.mil

10. SPONSOR/MONITOR'S ACRONYM(S)

AFWA

11. SPONSOR/MONITOR'S REPORT NUMBER(S)

12. DISTRIBUTION / AVAILABILITY STATEMENT

DISTRIBUTION STATEMENT A:
APPROVED FOR PUBLIC RELEASE; DISTRIBUTION UNLIMITED. CASE NUMBER: AFRL-2020-0743

13. SUPPLEMENTARY NOTES

14. ABSTRACT

Two-Beam Coupling (TBC) is a coherent interaction in which energy is transfered from one laser beam to another and has promising applications in real-time holography and coherent beam combing. We have recently shown efficient degenerate frequency TBC for counter-propagation geometries in isotropic two-photon absorbing media pumped with a nanosecond pulsed laser. When an interference pattern is generated in this media, single and two photon absorption initiates a population redistribution resulting in a holographic grating with the same modulation period and phase initially. However, due to temporal convolution of self- and cross-phase modulation, the grating will begin to shift in time relative to the interference pattern thus allowing coherent energy transfer to evolve. A comprehensive theoretical and numerical model is presented consistent with empirical results and historical observations of both energy and phase coupling. Numerical simulations indicate the presence self-oscillation due to nonlinear phase wrapping and strong excited state absorption inhibit energy transfer in a co-propagating geometry. However with proper temporal phase conditioning and choice of medium thickness, significant energy transfer can be achieved in the co-propagating case.

15. SUBJECT TERMS

Holography, Nonlinear Optics, Two-Beam Coupling

16. SECURITY CLASSIFICATION OF:			17. LIMITATION OF ABSTRACT	18. NUMBER OF PAGES	19a. NAME OF RESPONSIBLE PERSON
a. REPORT	b. ABSTRACT	c. THIS PAGE			J. E. Slagle, AFIT/ENP
U	U	U	U	110	**19b. TELEPHONE NUMBER** *(include area code)* (937) 255-1829; jonathan.slagle.2@us.af.mil

Standard Form 298 (Rev. 8–98)
Prescribed by ANSI Std. Z39.18